Laser-Microstructured Copper Reveals Selectivity Patterns in the Electrocatalytic Reduction of CO2

Journal Article

Author(s):
Veenstra, Florentine L.P.; Ackerl, Norbert [ID]; Martín, Antonio J.; Pérez-Ramírez, Javier

Selectivity Patterns in the Electrocatalytic Reduction of CO_2 Revealed by Laser-Microstructured Copper

Florentine L.P. Veenstra,[1] Norbert Ackerl,[2] Antonio J. Martín,[1] Javier Pérez-Ramírez[1,3,*]

[1] Institute for Chemical and Bioengineering, Department of Chemistry and Applied Biosciences, ETH Zürich, 8093 Zürich, Switzerland
[2] Institute for Machine Tools and Manufacturing, Department of Mechanical and Process Engineering, ETH Zürich, 8005 Zürich, Switzerland
[3] Lead contact
*Correspondence: jpr@chem.ethz.ch

SUMMARY

The strategy of engineering the local chemical environment to direct selectivity in the electroreduction of CO_2 toward value-added products is only qualitatively understood. The unfeasibility of local concentration measurements and the limited applicability of simulations to practical systems hinder more precise guidelines. Herein, we quantify the impact of the (electro)chemical environment on the selectivity pattern using microstructured Cu electrodes prepared by ultra-short pulse laser ablation. We created regularly distributed micro-probes and assessed their product distributions at distinct overpotentials. The regular geometry enabled the accurate simulation of the local pH and CO_2 concentration. Selectivity maps useful for mechanistic and applied studies emerged. They reveal clear patterns for C_1-C_3 products suggesting novel insights such as the presence of two reaction mechanisms for propanol. The effect on the selectivity pattern of operation parameters such as enhanced mass transport and electrolyte composition was also predicted by the maps.

Keywords: Electrocatalysis, CO_2 reduction, oxide-derived Cu, laser ablation, microfabrication, local electrochemical environment, selectivity patterns, reaction mechanism

INTRODUCTION

The electrocatalytic CO_2 reduction reaction (eCO_2RR) toward fuels and chemicals in aqueous media must still overcome technological challenges to contribute towards a sustainable, circular economy. The lack of selectivity control on copper-based systems stands out among them, since copper is the only material known to promote at appreciable rates value-added products such as hydrocarbons, alcohols, and aldehydes.[1-3] The insufficient understanding of the variables to be optimized hinders precise strategies for catalyst design, operation conditions, and electrode engineering.[4,5]

Historically, research in this field has been focused on materials development[6,7] but the recent recognition of the local (electro)chemical environment as a key directing agent for selectivity has opened new avenues. The applied potential and the surface coverage of H and CO_2 are central parameters influencing the eCO_2RR and the competing hydrogen evolution reaction (HER). However, their separated analysis is unattainable, as they are intertwined in the double layer region by the carbonate chemical equilibria, diffusion processes, and the interaction of charged species in the intense electric field.[4] Despite the complexity involved, literature shows how activity and/or selectivity can be successfully enhanced via locally tuned electric fields,[8] highly alkaline environments,[9,10] mixed chemical-electrocatalytic reduction routes,[11] or free cationic/anionic species present.[12,13] In this context, rationalization efforts have become necessary to translate these observations into quantitative guidelines for the optimization of the local environment. These efforts are currently focused on C_1 and C_2 products,[4,14-16] while there are virtually no indications for more complex ones.

Ethylene formation is a prominent example. The fact that its selectivity can be improved in a practical gas diffusion electrode from 30% to ca. 70% upon optimization of mass transport and electrolyte pH clearly reflects the sensitivity of this reaction to the environment.[9] In this regard, theoretical works predict the pH sensitivity of the rate-determining step in C-C

coupling due to a non-simultaneous proton-electron transfer.[17] This idea has led to diverse proposed mechanisms toward ethylene at different overpotentials with varying pH sensitivity[17,18] and its promotion by high local CO_2 concentration through enhanced CO coverage.[19] Neither the precise route(s) nor a quantitative description of the local environments under which they are promoted have been firmly established. Remarkably, ethanol is thought to share a significant portion of its reaction pathway with ethylene and therefore some of these features.[14,20,21] In parallel, local conditions may also affect the parasitic HER, for which high activity has been associated to enhanced mass transport properties.[22] Unfortunately, the relevance of quantifying the local electrochemical environment is in stark contrast with the ability to measure or model the concentrations of species in the vicinity of the electrode. This fact originates from technical limitations of operando techniques[23] and the usually complex morphology of the catalysts in the relevant micrometer scale, which provides results from forcibly simplistic models mostly with a qualitative value.[24,25] The lack of well-structured systems has not allowed a systematic study of mass transport, chemical equilibria, and local cationic buffer effects.[26] With this in mind, copper-based surfaces with a variable degree of control have been reported as in the case of foams[27,28] or mesostructured layers with variable thickness.[29] They have confirmed with limited quantification, for example, the improved selectivity toward C_2 products under severe mass transport limitations. A clever templating strategy allowed to experimentally link cylindrical nanoporosity and larger rates of C_2 products rationalized–through local concentration gradients and confinement effects.[30] Nonetheless, selectivity could not be linked to intrinsic physicochemical parameters but rather to the length of nanocavities.

Microfabrication can contribute to this need of describing selectivity patterns in terms of chemical environment descriptors by providing catalysts with controlled geometry. This set of techniques has been demonstrated through lithographic approaches to gather insights into the formation and nature of active sites in multicomponent systems[31,32] and into the operation of bifunctional catalysts.[33] In this study we identified ultra-short pulsed (USP, pulse duration from fs to ps) laser ablation[34,35] as the technique of choice for the development of model copper electrodes. Whereas nanosecond pulsed laser ablation is a well-established technique for nanoparticle synthesis,[36] USP laser ablation has only found application in the field of catalysis to enhance electrode roughness.[37] Its sub-micrometer resolution (mostly limited by diffraction) displays a large potential for precise structuring, arising from the small energy input per pulse that creates negligible heat affected zones.[38] This feature adds to rapid-processing[39] (up to 1 m^2 min^{-1}) and the ability to alter the chemical nature of the ablated surface when applied under reactive atmospheres.[40,41] We ablated copper foils using this platform to develop microstructured CuO electrodes amenable to product quantification. We designed them as a dense regular distribution of conical cavities (denoted as micro-probes) spanning a wide range of lengths.

The combination of applied potentials and micro-probe lengths imposed distinct local electrochemical environments due to concentration gradients arising from the electrochemical reactions, CO_2 and cation hydrolysis equilibria, and geometry. These environments could be quantitatively described after 3D simulations, which enabled the emergence of selectivity patterns in the form of maps for a variety of C_1-C_3 products expressed in terms of local CO_2 concentration and pH. Selectivity maps emerge as valuable resources for theoretical studies and as guiding tools toward optimized operation parameters.

RESULTS AND DISCUSSION

This section describes initially the preparation and characterization of microstructured copper electrodes and the associated selectivity patterns at different potentials. This set of results is subsequently used as input for 3D models enabling the quantification of the local chemical environment under eCO$_2$RR conditions. As a result, selectivity patterns for C_1-C_3 products emerge using the simulated local pH and CO_2 concentration as descriptors. Finally, a mechanistic discussion and an analysis of the influence of operation parameters based on obtained maps close the section.

Cu foils were initially pretreated by ablation of a 2 μm layer (LA-Cu-0) and subsequently patterned to create regular arrays of micro-probes with different length (LA-Cu-L). B) X-ray diffraction (XRD) patterns before (Cu) and after laser ablation (LA-Cu-0), C) X-ray photoelectron spectroscopy (XPS) spectra of LA-Cu-0 before and after electrolysis. D) Micrograph showing the periodically aligned micro-probes and a partially removed surface layer. E) Representative

Plasma Focused Ion Beam-Scanning Electron Microscopy (PFIB-SEM) cross-sectional micrograph of one micro-probe. Case shown: LA-Cu-100, after exposure to reaction conditions.

Fabrication and characterization of microstructured electrodes

The driving idea of this study is to enable the imposition of different local chemical environments under operation conditions keeping unaltered both the potential and the catalyst. To this end, we aimed to design model electrodes whose geometry could influence mass transport properties and thus the local concentrations of species. Inspired by monoliths widely applied in thermocatalytic processes,[42] we anticipated that the mean diffusion pathway between the active walls and the external environment would be controlled in a cylindrical or conical micro-reactor by its length. The fabrication of their analogues in a copper foil demanded the ability to create regular cavities at the micrometer scale the relevant in a practical catalytic layer in a gas diffusion electrode.[43] Based on this, we applied USP laser ablation to transform copper foils into model electrodes, as shown in **Figure 1**. The ablation was performed in air, given the enhanced production of complex products generally observed over oxidic copper surfaces.[3]

In more detail, a first ablation step pretreated the foils by removing ca. 2 μm of material to produce a submicrometrically roughened surface called LA-Cu-0 (where "0" denotes zero, **Figure 1A** and **S1**) whose composition was identified as CuO after X-ray diffraction and X-ray photoelectron spectroscopy analyses (**Figure 1B** and **Figure 1C and S2**, respectively). Importantly, to understand the effect on the catalytic performance introduced by the USP laser ablation treatment, we first compared selectivity patterns under CO_2-saturated 0.1 M $KHCO_3$ (pH 6.8) for the unprocessed Cu foils and LA-Cu-0 surface (**Figure 2**).

The results show that the application of laser ablation brings a modest influence for carbon monoxide, formate, and ethylene (**Figure 2A**) but enhances the formation of alcohols and suppresses the formation of acetate (**Figure 2B**). The post reaction characterization of LA-Cu-0 confirmed the expected reduction of CuO into Cu (**Figure 1B** and **Figure 1C** and **S2**). In this regard, improved rates toward ethylene and/or alcohols on oxide-derived Cu have been repeatedly reported (though not in all cases[44,45]) but their origin is subject to a vivid debate.[3] Modified selectivity has been linked to the formation upon reduction of the oxide of particular active sites such as grain boundaries,[46,47] remaining interstitial oxygen,[48] or low-coordinated Cu sites.[49] Nonetheless, the idea of the chemical environment primarily directing the selectivity over these materials due to their unusually large roughness (provoking strong local pH and CO_2 concentration gradients) has been gaining relevance and is now openly claimed.[3,30,50] In accordance, we notice that the catalytic performances in our case differ mainly at high potentials (i.e., larger currents) and that ablation increased the roughness by a factor of 3 (**Table S1**) due to redeposition of copper as debris (**Figure S1**).

The laser ablated LA-Cu-0 surface was subsequently microstructured to obtain the set of model electrodes. A dense regular distribution of conical micro-probes (**Figure S3**) was prepared by a circular hatch of the laser beam (see **Figure 1A** and the **Supplemental Experimental Procedures** for a full description). We kept their diameter and pitch constant (**Figure 1D** and **1E**), whereas their length was controlled by the number of incident laser pulses. The resulting electrodes (2.25 cm²) contained ca. 92 000 micro-probes and are denoted after their length (LA-Cu-L, with L= 0, 20, 40, 60, 100, 130 μm). This strategy achieved a quasi-linear dependency of the exposed surface area with L, in spite of some deviations from the conical shape due to reflections of the laser beam, as disclosed by microcomputed tomography (**Figure S4**). In regard to their chemical nature, all LA-Cu-L electrodes showed similar composition (**Figure S5**), confirming the feasibility of this approach toward a set of chemically identical microstructured electrodes with favorable catalytic performance enabling the study of a variety of products.

Revealing selectivity patterns by varying applied potential and electrode geometry

Qualitatively, we expected larger L and more negative potentials to increase the average local pH and reduce the concentration of CO_2. Following this reasoning, the performance of the microstructured electrodes was evaluated at different potentials (V = –0.6, –0.8, –1.05, –1.3 V vs. RHE) as described in the **Supplemental Experimental Procedures**. Exposure to reaction conditions did not alter the structure of these electrodes as revealed by SEM (**Figure S6**). Cyclic voltammetries did not show unexpected redox signals or degradation either (**Figure S7**). We carefully quantified products with modest Faradaic efficiencies (FE) in

view of their value to discuss potential mechanistic routes (see **Figure S8** and **Table S2**). The set of major products was common across all conditions (**Figure 2** and **Table S3**).

Selectivity patterns are presented as maps in **Figure 3** for representative C_1 (formate), C_2 (ethanol), and C_3 (propanol) products and for the rest in **Figure S9**. Variations in selectivity at a fixed potential must be ascribed to the different geometry of the electrodes. A quick inspection reveals the predominance of C_1 products at low potentials and of C_2 at larger ones (**Figure S9**), as early reported over non-structured Cu,[51] with minor impact of L. Turning into particular products, formate (**Figure 3**) was produced with relatively high selectivity (30-40%) over a wide zone at all L values with no clearly discernible pattern. In contrast, CO was formed with no exception at low quantities (**Figure S9**, **Table S3**), as it is the case for oxide-derived Cu catalysts with mild roughness promoting complex products.[50] More interestingly, the maps for ethylene (**Figure 3**) and ethanol (**Figure S9**) resemble each other considerably, suggesting partially shared mechanistic routes as already proposed by theoretical studies.[4] **Figure S10** provides the corresponding maps for ethanol and ethylene referred to the standard hydrogen electrode (SHE) to account for the claimed pH dependency of the proposed rate determining C-C coupling step.[17] Finally, propanol (**Figure 3**) is favored (6-7% FE) over two different regions partly overlapping with the C_2 ones, thus suggesting similarities among mechanisms.[52,53]

Even though these results established the feasibility of varying the geometry of the electrodes to obtain selectivity patterns, these maps show very limited practical relevance at this stage, since they reflect the performance of this particular set of electrodes under certain operation conditions. We thus aimed to obtain selectivity maps of more general applicability by translating potential and L into average local pH and CO_2 concentration in the interior of the micro-probes.

Modelling the local chemical environment under operation conditions on microstructured electrodes

The required quantitative description of the local chemical environment was attained by computational modelling. The set of experimental results comprising current densities (**Table S4**) and Faradaic efficiencies (**Table S2** and **S3**) alongside the geometry of the electrodes were used as input for 3D simulations targeting the concentrations and fluxes of relevant species on the flat surface and within the interior of the micro-probes. Most of the assumptions contained in our model are comparable to those found in other works developed over more ill-defined[24] or flat[54] surfaces (**Tables S5** to **S7**). We nonetheless remark that the model considers the local buffer effect of hydrolysis of cations (**Table S8**) as proposed by Singh et al.[55] The **Supplemental Experimental Procedures** provides a detailed description of the model.

The modelled electrolyte included three regions (**Figure 4A**). The first one encompasses the volume contained in the micro-probe under analysis as defined in **Figure 1** and **Figure S4**. To include the potential effect of neighbor micro-probes, the 8 adjacent were added as the second region. The third region accounts for the diffusion layer, as it was considered the dominant mass transport mechanism at this scale. Its thickness accounts for the degree of convection and can be tuned to simulate enhanced (small thickness) or impeded (large thickness) mass transport in the bulk of the solution. Its value (50 μm) reflects the mild convection imposed in the cathodic chamber by CO_2 bubbling (see **Supplemental Experimental Procedures** for a more extended description). The concentration and flux of OH^-, CO_2, HCO_3^-, and CO_3^{2-} species were calculated at steady state upon considering the interplay between the eCO_2RR and HER activities (**Table S4**), the chemical equilibria of carbonate species (**Table S6**), the local buffer effect of the hydrolysis of cations, and diffusion (**Table S7**).

As boundary conditions we imposed bulk concentrations at the free end of the diffusion layer ($z = -50$ μm in **Figure 4A**), zero flux for non-reactive species on the copper surfaces, zero flux for all species on the lateral walls of the diffusion layer for symmetry reasons, and equilibrium for the hydrolysis of cations next to the copper surfaces, to account for this effect relevant at the atomic scale (see the **Supplemental Experimental Procedures** for calculation of the associated pKa). Critically, experimental partial current densities enabled to impose the flux of OH^- and CO_2 as the boundary condition on the copper surfaces. In more detail, we considered the CO_2 consumption rate as linearly related to its concentration and the HER activity to increase linearly along the z-axis (in line with reports claiming increased HER with decreasing local CO concentration[56]), adapting the procedure developed by Raciti et al.[24] The

reaction rate constants for both the HER and eCO$_2$RR were determined after imposing the matching of the measured current density corrected by the double layer capacitance (**Table S1**) and the current density obtained after integrating the assumed reaction rates over the copper surfaces (see **Supplemental Experimental Procedures** for an extended description). The catalytic behavior of the ablated but non-microstructured surface (i.e., that between micro-probes) was considered equal to that of Cu-LA-0 (see **Figure 2**). We notice that the fragmented mechanistic information available made us consider the reaction rates of all products to vary in the same manner along the z-coordinate, which may not accurately reflect reality. This fact constitutes an opportunity for refinement in the future.

The populated set of results with 3D character and the complexity of the modelled volume demanded a strategy enabling a straightforward analysis. In view of the geometry of the micro-probes, we investigated if the concentrations could be treated as 1D without loss of generality. In fact, **Figure S11** demonstrates that pH and CO$_2$ concentration can be accurately described as unidimensional variables solely dependent on the z-coordinate in the interior of the micro-probes. In addition, the negligible mutual influence between adjacent probes was also unveiled. On a lateral note, a detailed analysis of the modeled flux of species revealed that L and potential can be used as descriptors of the CO$_2$ flux, exposing the interplay among geometry, potential, and mass transport (see **Figures S12**, **S13**, and **S14**).

Finally, we sought to quantify local concentrations of protons and CO$_2$ for each combination of potential and L. **Figures 4B-E** show representative cases at low (–0.6 V) and high (–1.3 V) potentials for short (LA-Cu-40) and long (LA-Cu-100) micro-probes. The combination of low potential and short length (**Figure 4B**) led to negligible depletion of CO$_2$ along the axis but to a significant pH increase of more than one unit over the bulk at z = L. The application of low potentials to longer micro-probes (**Figure 4D**) did not have a strong impact on the concentration of CO$_2$ either, showing the ability of the buffered electrolyte and short diffusion paths to keep a homogeneous concentration at modest current densities (**Table S4**). However, the effect on the pH is even more noticeable. In the case of high potentials, short micro-probes (**Figure 4C**) also exhibited relatively high concentrations of CO$_2$ with the expected variation on pH. In contrast, long micro-probes (**Figure 4E**) developed large gradients of CO$_2$ concentration and pH along the axis (pH~10.2, [CO$_2$] = 12 mol m^{-3} at z = 100 μm), suggesting a wide range of chemical environments at work. We can thus conclude that at low potentials L can be used to tune the local pH while keeping a high and approximately constant CO$_2$ concentration throughout the volume, whereas at high potentials this strategy fails for large L values.

After these results, the pH and CO$_2$ concentration averaged over the z-axis were taken as representative descriptors for further analyses. Maps relating these variables with L and potential are shown in **Figure S15**. A quick inspection reveals that the average CO$_2$ concentration high approximately constant in all experiments except for the combination of large L values and high potentials, whereas the average pH is mostly dependent on the applied potential and shows a wide plateau at pH 9-9.3 between –0.8 and –1.2 V vs. RHE.

Mapping selectivity versus chemical environment descriptors

As soon as potential and micro-probe length could be correlated to average pH and CO$_2$ concentration, we mapped selectivity values versus them to expose patterns for each of the main products (**Figure 5**). As targeted, these maps are independent of the particular experimental setup used and thus reflect intrinsic trends of eCO$_2$RR on Cu materials. To confirm the kinetic nature of the maps, we mapped the current density associated to formation of carbon products in **Figure S16**. From the lack of plateau regions it can be inferred that mass transport limitations do not play a relevant role and thus the observed patterns can be largely ascribed to mechanistic differences. In agreement with the lack of limiting current densities, average CO$_2$ concentrations were in all cases larger than 65% of the bulk value (34 mol m^{-3}, **Table S9**). At this point, we highlight the relevance of the local buffer effect of the hydrolysis of cations for an accurate assessment of the local chemical environment. The model proposed by Singh et al.[55] and incorporated into our calculations introduces a local source of protons through a fast hydrolysis equilibrium with a pKa of up to ~8 under high overpotentials (see **Supplemental Experimental Procedures**). **Figure S17** compares maps shown in **Figure 5** with the equivalent ones where this effect is disregarded. Hydrolysis plays a modest role at mild conditions but becomes a large driver of the chemical environment at high overpotentials.

We now aim to provide a general perspective for all products by overlaying regions showing high selectivity. The resulting map after mathematical smoothing is displayed in **Figure 6** (see **Figure S18** for the unprocessed version including experiments modelled). Some relations among products become explicit on this representation, such as the intermediate position of the C_3 region between C_1 and C_2 at mild pH and high concentration of CO_2, where C_2 formations begin to rise but C_1 are still produced with appreciable activity. This puts forward that mild overpotentials and good mass transport conditions may favor C_3 formation. In this regard, a second region for propanol (FE = 4% in **Figure 7**) overlapping with the corresponding region for ethylene was identified by the mathematical treatment, suggesting a second mechanism at higher pH values where ethylene may play the role of intermediate. Finally, the lack of correlation between acetate and ethanol discards an impact of chemical routes (Cannizzaro-type reactions) in the formation of the latter.[11]

Mechanistic relevance of selectivity maps

In regard to mechanistic considerations for specific products in maps displayed in **Figure 5**, the formate map points to its preferential formation under a relatively wide range of chemical environments (pH 8.0-9.8 and $[CO_2] > 20$ mol m^{-3}), suggesting a poorly sensitive mechanism. Carbon monoxide seems to share affinity for high concentrations of CO_2 constrained to a less alkaline pH range (< 9). This observation agrees with the promotion of formate over carbon monoxide reported as the pH increases.[25] In addition, carbon monoxide shows lower selectivity in regions where C_2 products develop appreciably, in line with its accepted role of key intermediate.

The ethylene map presents two regions that call for a discussion on the light of proposed mechanisms associated to high and low overpotentials.[18,57,58] The first region finds at a narrow range with high pH values and contains a maximum (FE = 35%, $[CO_2]$ = 22 mol m^{-3}, pH 9.9, see **Table S3** and **Table S9**) for LA-Cu-20 exposed to −1.3 V. In principle, this region could be reasonably ascribed to one of the high-overpotential mechanisms with strong pH dependence proposed either on Cu(111) or Cu(100). However, the small amount of methane produced (FE = 3% at the maximum, **Table S3**) suggests additional route(s) to those proposed by the groups of Koper[57] or Goddard.[58] Similarly, the route proposed by Head-Gordon et al.[59] is a problematic alternative in view of the small amount of acetate detected (FE~0.1%, **Table S2**). Interestingly, the other region with no distinct pH dependence at larger CO_2 concentrations (maximum at FE~30%, $[CO_2]$ =28 mol m^{-3}, pH 9.1, LA-Cu-130 operated at −0.8 V) might correspond to a low-overpotential route. Indeed, the relatively large amount of acetate (FE = 1-3%) at the upper part of this region is compatible with some contribution arising from the Head-Gordon route.

The consideration of the ethanol pattern sheds additional light on this mechanistic discussion, since it largely resembles that of ethylene (also observed in **Figure 3**). More specifically, the formation of ethylene glycol (FE~1%, $[CO_2]$ =26 mM, pH 9.8) in the upper part of the region associated to larger CO_2 concentrations further supports the Head-Gordon pathway. However, this association cannot be extended to lower pH values, where the maximum for ethanol (overlapping with the ethylene one) is located (FE = 9.8%, $[CO_2]$ =28 mol m^{-3}, pH 9.1). Regarding the other region, at higher pH values, both maxima also overlap (FE$_{ethanol}$ = 13.4%) and similarly, a tentative assignment of the predominant mechanistic route is precluded by the trace levels of minor products quantified (**Table S2**). We thus conclude that despite the qualitative agreement, none of the proposed mechanistic routes for ethylene and/or ethanol closely match our observations, suggesting unaccounted pathways. Interestingly, the propanol map also discloses a discernible pattern.

Regrettably, the mechanistic discussion based on literature is to date forcibly limited for C_3 products due to their yet largely unexplored reaction networks. Acetaldehyde has been recently proposed as a key intermediate toward propanol through its dehydrogenative adsorption as methyl carbonyl.[26] However, the very low FE observed for acetaldehyde in the region where the propanol one peaks (<0.1%, **Tables S2** and **S3**) makes it reasonable to assign a secondary relevance to this route in our study. Ethylene has also been proposed as a key intermediate for the formation of propanol.[53,60,61] Our results reveal the high sensitivity of propanol formation to the chemical environment. It shows a nearly pH-independent optimal region at high CO_2 concentrations that overlaps with ethylene (maximum at FE = 5.4%, $[CO_2]$ =28 mol m^{-3}, pH 9.1) thus supporting their mechanistic relation. Given the dependency of eCO$_2$RR equilibrium potential with the concentration of protons and CO_2, we thus turned to investigate the overpotentials at which propanol was optimized. The

overpotentials could be calculated from the Nernst equation upon correcting the standard reduction potential with the simulated concentration of species (**Figure S9**). The selectivity map in terms of local pH and overpotential (**Figure S19**) exhibits two favorable regions at mid (0.7 V) and high (1.1 V) overpotentials, predicting two mechanisms at work that have not been explored in the literature.

Influence of mass transport and electrolyte

In this section we assess under which conditions and how selectivity maps may help defining optimal operation conditions for selectivity control. Maps contribute to rationalize the largely reported sensitivity of eCO_2RR to the reactor configuration and operation conditions. Cathodic catalysts in artificial leaves[62,63] usually operate in contact with liquid electrolyte and display current densities below 10 mA cm^{-2} comparable to those reported in **Table S4** due to the limited energy density of sunlight (ca. 1 kW m^{-2}). CO_2 electrolyzers fed by grid electricity, on the other hand, are typically designed based on gas diffusion electrodes (GDE) whose geometric current densities may reach hundreds of mA cm$_{geo}^{-2}$.[43] Nevertheless, the large electrochemical surface area typically reported over porous catalytic layers[64] of more than 30 m^2 g$_{metal}^{-1}$ leads to current densities of tens of mA cm$_{metal}^{-2}$ for typical catalyst loadings of 1 mg$_{metal}$ cm$_{geo}^{-2}$. Selectivity maps in **Figure 5** are thus directly applicable to devices such as artificial leaves and may reasonably describe the main features of CO_2 electrolyzers operated below extreme current densities.

The transport of CO_2 to the active sites is typically enhanced either by the use of stirring in liquid medium or the use of a GDE configuration. To understand the changes in the local chemical environment associated to enhanced mass transport, we exposed selected Cu-LA-L electrodes with very different geometry (L=40,100) to potentials where mass transport expectedly plays a role (V = −1.05, −1.3 V vs. RHE) under mild stirring in 0.1 M $KHCO_3$. These experiments were computationally treated by considering 20 µm as the thickness of the diffusion layer (**Figure 4A**) after its estimation using the Levich equation.[65] Local pH and CO_2 concentrations showed remarkable differences when compared with the equivalent experiment without stirring (see **Figure S20**). **Figure 7A** displays the positions of representative examples (LA-Cu-100, −1.05 V vs. RHE with and without stirring denoted as K_s^+ and K^+, respectively) in the global selectivity map. Stirring increases the average local CO_2 concentration from 22 to 29 mol cm^{-3} and concomitantly decrease the average pH from 9.6 to 9.2 (see **Figure 7A** and **7B**, and **Table S9**). Remarkably, the selectivity pattern predicted for the stirring experiment by the position of K_s^+ in the map (dashed bars in **Figure 7C**) closely predicted the experimental (solid bars). The large discrepancy found for ethylene may be related to the large gradients in its Faradaic efficiency associated to that region (see **Figure 5**), making the predicted value very sensitive to small uncertainties in simulated results.

The electrolyte of choice in the eCO_2RR plays a critical role in both activity and selectivity, which has been linked to the local effect of the free cationic species in the vicinity of the catalyst surface.[66] Larger cations are expected to show a lower pKa for their hydrolysis and a concomitant enlarged buffer capability (see **Supplemental Experimental Procedures** for details on the calculations). We exposed Cu-LA-L electrodes (L=0, 40, 100) to −1.05 V vs. RHE in 0.1 M $CsHCO_3$ (no stirring applied) and simulated the local environment upon introducing Cs^+ hydrolysis equilibrium parameters in the model. **Figure S20** illustrates how local pH and CO_2 concentrations varied notably along the axis of the micro-probes with respect to the equivalent experiments in 0.1 $KHCO_3$, facilitating a larger concentration of CO_2 and decreased pH. **Figure 7A** displays the position of the representative LA-Cu-100 exposed to −1.05 V vs. RHE (denoted as Cs^+, **Table S9**). The use of $CsHCO_3$ allowed an increased CO_2 concentration (30 vs. 22 mol cm^{-3}) and reduced pH (8.8 vs. 9.6). Similarly to the case of K_s^+, the position of Cs^+ predicted with notable accuracy the experimental distribution of products (**Figure 7C**) with the exception of formate, for the same reasons explained for ethylene in the case of stirring. It is apparent from the comparison between K_s^+ and Cs^+ that enhanced mass transport and electrolyte buffering effect play a somewhat similar role in varying the local chemical environment, though the latter is dependent on catalyst surface charge and thus on the potential.

From a more general perspective, these results reflect the ability of selectivity maps to account for the effect of operation conditions on the selectivity pattern. Given a target product, this feature may be thus used to orient basic design parameters. For example, the use of an electrolyte with mild cationic buffer effect such as $KHCO_3$ in combination with a mild stirring seems an advisable combination toward the selective production of propanol.

Conclusions

The application of microstructuring and advanced modeling enabled to quantify the relation between selectivity and a broad range of chemical environments in the eCO_2RR on Cu. We unveil selectivity maps for the main C_1-C_3 products in terms of local CO_2 concentration and pH. This was achieved by testing microstructured Cu foils processed by laser ablation followed by simulations facilitated by the regular geometry of the electrodes. Selectivity maps disclosed clear patterns shedding light on open mechanistic queries. Ethylene and ethanol patterns could not be entirely accounted for by proposed mechanisms, whereas the role of ethylene as intermediate toward propanol is compatible with our results that suggest the presence of two mechanisms at mid- and high overpotentials. From an operational perspective, selectivity maps successfully predicted the influence of operation conditions such as stirring or the use of different electrolyte on the product distribution, suggesting their potential to guide process design.

EXPERIMENTAL PROCEDURES

Resources availability

Lead contact. Further information and requests for resources and reagents should be directed to and will be fulfilled by Javier Pérez-Ramírez (jpr@chem.ethz.ch)

Materials availability. This study did not generate new unique reagents.

Data and code availability. The published article includes all datasets generated or analyzed during this study.

Microstructuring, characterization, and modelling

Copper foils (0.3 mm, 20 mm x 20 mm) were processed using ultra-short pulsed laser ablation[34,35] to impose geometry and chemical composition. The modified copper oxide electrode (2.25 cm²) comprised ca. 92000 conical micro-probes with different lengths (0, 20, 40, 60, 100, 130 µm). Electrodes were tested in a two-compartment custom-made gastight flow-cell with a three-electrode configuration in 0.1 M $KHCO_3$ or 0.1 M $CsHCO_3$ under continuous CO_2 bubbling with and without stirring (pH 6.8). The selectivity for gas products was determined by GC (H_2, CO, CH_4, C_2H_4) and by ¹H-NMR for liquid ones ($HCOO^-$, $C_2H_3OO^-$, C_2H_5OH, C_3H_7OH, CH_3OH, C_2H_4O, $C_2H_6O_2$, C_3H_6O). The morphology of catalytic surfaces was assessed by SEM, optical microscopy, microcomputed tomography and PFIB-SEM, whereas the chemical composition was determined by XRD and XPS. All simulations were accomplished using a 3D finite element method incorporating a MUMPS type solver in the COMSOL® platform. Full details can be found in the **Supplemental Experimental Procedures**.

SUPPLEMENTAL INFORMATION

Supplemental information can be found online at (...).

AUTHOR CONTRIBUTIONS

Conceptualization, A.J.M. and J.P.R.; Methodology, F.L.P.V. and A.J.M.; Formal Analysis, F.L.P.V. and A.J.M.; Investigation, F.L.P.V.; Resources, N.A.; Writing – Original Draft, F.L.P.V., N.A. and A.J.M.; Writing – Review & Editing, F.L.P.V., A.J.M. and J.P.R.; Visualization, F.L.P.V. and A.J.M.; Supervision, J.P.R.; Project Administration, F.L.P.V.; Funding Acquisition, J.P.R.

DECLARATION OF INTERESTS

The authors declare no competing interests.

REFERENCES AND NOTES

1. Martín, A.J., and Pérez-Ramírez, J. (2019). Heading to Distributed Electrocatalytic Conversion of Small Abundant Molecules into Fuels, Chemicals, and Fertilizers. Joule *3*, 2602–2621.

2. Kuhl, K.P., Cave, E.R., Abram, D.N., and Jaramillo, T.F. (2012). New insights into the electrochemical reduction of carbon dioxide on metallic copper surfaces. Energy Environ. Sci. *5*, 7050-7059.

3. Nitopi, S., Bertheussen, E., Scott, S.B., Liu, X., Engstfeld, A.K., Horch, S., Seger, B., Stephens, I.E.L., Chan, K., Hahn, C., Nørskov, J.K., Jaramillo, T.F., and Chorkendorff, I. (2019). Progress and perspectives of electrochemical CO_2 reduction on copper in aqueous electrolyte. Chem. Rev. *119*, 7610–7672.

4. Birdja, Y.Y., Pérez-Gallent, E., Figueiredo, M.C., Göttle, A.J., Calle-Vallejo, F., and Koper, M.T.M. (2019). Advances and challenges in understanding the electrocatalytic conversion of carbon dioxide to fuels. Nat. Energy *4*, 732–745.

5. Larrazábal, G.O., Martín, A.J., and Pérez-Ramírez, J. (2017). Building blocks for high performance in electrocatalytic CO_2 reduction: materials, modification strategies, and device engineering. J. Phys. Chem. Lett. *8*, 3933–3944.

6. Vasileff, A., Xu, C., Jiao, Y., Zheng, Y., and Qiao, S.Z. (2018). Surface and interface engineering in copper-based bimetallic materials for selective CO_2 electroreduction. Chem *4*, 1809–1831.

7. Zhang, L., Zhao, Z.-J., and Gong, J. (2017). Nanostructured materials for heterogeneous electrocatalytic CO_2 reduction and their related reaction mechanisms. Angew. Chem. Int. Ed. *56*, 11326–11353.

8. Liu, M., Pang, Y., Zhang, B., De Luna, P., Voznyy, O., Xu, J., Zheng, X., Dinh, C.T., Fan, F., Cao, C., de Arquer, F.P.G., Safaei, T.S., Mepham, A., Klinkova, A., Kumacheva, E., Filleter, T., Sinton, D., Kelley, S.O., and Sargent, E.H. (2016). Enhanced electrocatalytic CO_2 reduction via field-induced reagent concentration. Nature *537*, 382–386.

9. Dinh, C.-T., Burdyny, T., Kibria, M.G., Seifitokaldani, A., Gabardo, C.M., García de Arquer, F.P., Kiani, A., Edwards, J.P., De Luna, P., Bushuyev, O.S., Zou, C., Quintero-Bermudez, R., Pang, Y., Sinton, D., and Sargent, E.H. (2018). CO_2 electroreduction to ethylene via hydroxide-mediated copper catalysis at an abrupt interface. Science *360*, 783–787.

10. Varela, A.S., Kroschel, M., Reier, T., and Strasser, P. (2016). Controlling the selectivity of CO_2 electroreduction on copper: The effect of the electrolyte concentration and the importance of the local pH. Catal. Today *260*, 8–13.

11. Birdja, Y.Y., and Koper, M.T.M. (2017). The importance of Cannizzaro-type reactions during electrocatalytic reduction of carbon dioxide. J. Am. Chem. Soc. *139*, 2030–2034.

12. Singh, M.R., Kwon, Y., Lum, Y., Ager, J.W., and Bell, A.T. (2016). Hydrolysis of electrolyte cations enhances the electrochemical reduction of CO_2 over Ag and Cu. J. Am. Chem. Soc. *138*, 13006–13012.

13. Chen, C.S., Wan, J.H., and Yeo, B.S. (2015). Electrochemical reduction of carbon dioxide to ethane using nanostructured Cu_2O-derived copper catalyst and palladium(II) chloride. J. Phys. Chem. C *119*, 26875–26882.

14. Kas, R., Kortlever, R., Yilmaz, H., Koper, M.T.M., and Mul, G. (2015). Manipulating the hydrocarbon selectivity of copper nanoparticles in CO_2 electroreduction by process conditions. ChemElectroChem *2*, 354–358.

15. Hori, Y., Murata, A., and Takahashi, R. (1989). Formation of hydrocarbons in the electrochemical reduction of carbon dioxide at a copper electrode in aqueous solution. J. Chem. Soc. Faraday Trans. *85*, 2309–2326.

16. Raciti, D., Mao, M., Park, J.H., and Wang, C. (2018). Local pH effect in the CO_2 reduction reaction on high-surface-area copper electrocatalysts. J. Electrochem. Soc. *165*, F799–F804.

17. Calle-Vallejo, F., and Koper, M.T.M. (2013). Theoretical considerations on the electroreduction of CO to C_2 Species on Cu(100) electrodes. Angew. Chem. Int. Ed. *52*, 7282–7285.

18. Luo, W., Nie, X., Janik, M.J., and Asthagiri, A. (2016). Facet dependence of CO_2 reduction paths on Cu electrodes. ACS Catal. *6*, 219–229.

19. Liu, X., Schlexer, P., Xiao, J., Ji, Y., Wang, L., Sandberg, R.B., Tang, M., Brown, K.S., Peng, H., Ringe, S., Hahn, C., Jaramillo, T.F., Nørskov, J.K., and Chan, K. (2019). pH effects on the electrochemical reduction of $CO_{(2)}$ towards C_2 products on stepped copper. Nat. Commun. 32, 1-10.

20. Hahn, C., Hatsukade, T., Kim, Y.-G., Vailionis, A., Baricuatro, J.H., Higgins, D.C., Nitopi, S.A., Soriaga, M.P., and Jaramillo, T.F. (2017). Engineering Cu surfaces for the electrocatalytic conversion of CO_2: Controlling selectivity toward oxygenates and hydrocarbons. Proc. Natl. Acad. Sci. U.S.A *114*, 5918–5923.

21. Kwon, Y., Lum, Y., Clark, E.L., Ager, J.W., and Bell, A.T. (2016). CO_2 electroreduction with enhanced ethylene and ethanol selectivity by nanostructuring polycrystalline copper. ChemElectroChem *3*, 1012–1019.

22. Lim, C.F.C., Harrington, D.A., and Marshall, A.T. (2017). Effects of mass transfer on the

electrocatalytic CO_2 reduction on Cu. Electrochim. Acta *238*, 56–63.

23. Fuladpanjeh-Hojaghan, B., Elsutohy, M.M., Kabanov, V., Heyne, B., Trifkovic, M., and Roberts, E.P.L. (2019). In-pperando mapping of pH distribution in electrochemical processes. Angew. Chem. Int. Ed. *58*, 16815–16819.

24. Raciti, D., Mao, M., and C. Wang. (2018). Mass transport modelling for the electroreduction of CO_2 on Cu nanowires. Nanotechnology *29*, 1-10.

25. Bumroongsakulsawat, P., and Kelsall, G.H. (2014). Effect of solution pH on CO: formate formation rates during electrochemical reduction of aqueous CO_2 at Sn cathodes. Electrochim. Acta *141*, 216–225.

26. Chang, X., Malkani, A., Yang, X., and Xu, B. (2020). Mechanistic Insights into Electroreductive C-C Coupling between CO and Acetaldehyde into Multicarbon Products. J. Am. Chem. Soc. *142*, 2975–2983.

27. Rahaman, M., Dutta, A., Zanetti, A., and Broekmann, P. (2017). Electrochemical reduction of CO_2 into multicarbon alcohols on activated Cu mesh catalysts: an identical location (IL) study. ACS Catal. *7*, 7946–7956.

28. Dutta, A., Rahaman, M., Mohos, M., Zanetti, A., and Broekmann, P. (2017). Electrochemical CO_2 conversion using skeleton (sponge) type of Cu catalysts. ACS Catal. *7*, 5431–5437.

29. Song, H., Im, M., Song, J.T., Lim, J.-A., Kim, B.-S., Kwon, Y., Ryu, S., and Oh, J. (2018). Effect of mass transfer and kinetics in ordered Cu-mesostructures for electrochemical CO_2 reduction. Appl. Catal. B Environ. *232*, 391–396.

30. Yang, K.D., Ko, W.R., Lee, J.H., Kim, S.J., Lee, H., Lee, M.H., and Nam, K.T. (2017). Morphology-directed selective production of ethylene or ethane from CO_2 on a Cu mesopore electrode. Angew. Chem. Int. Ed. *56*, 796–800.

31. Larrazábal, G.O., Shinagawa, T., Martín, A.J., and Pérez-Ramírez, J. (2018). Microfabricated electrodes unravel the role of interfaces in multicomponent copper-based CO_2 reduction catalysts. Nat. Commun. 9:1477, 1-10.

32. Veenstra, F.L.P., Martín, A.J., and Pérez-Ramírez, J. (2019). Nitride-derived copper modified with indium as a selective and highly stable catalyst for the electroreduction of carbon dioxide. ChemSusChem *12*, 3501–3508.

33. Lum, Y., and Ager III, J.W. (2018). Sequential catalysis controls selectivity in electrochemical CO_2 reduction on Cu. Energy Environ. Sci. *11*, 2935–2944.

34. Ackerl, N., Warhanek, M., Gysel, J., and Wegener, K. (2019). Ultrashort-pulsed laser machining of dental ceramic implants. J. Eur. Ceram. Soc. *39*, 1635–1641.

35. Ackerl, N., Boerner, P., and Wegener, K. (2019). Toward application of hierarchical structures by ultrashort pulsed laser ablation. J. Laser Appl. *31*, 022501, 1-8.

36. Fang, H., Yang, J., Wen, M., and Wu, Q. (2018). Nanoalloy materials for chemical catalysis. Adv. Mater. *30*, 1705698, 1-10.

37. Lange, K., Schulz-Ruhtenberg, M., and Caro, J. (2017). Platinum electrodes for oxygen reduction catalysis designed by ultrashort pulse laser structuring. ChemElectroChem *4*, 570–576.

38. Weber, R., Graf, T., Freitag, C., Feuer, A., Kononenko, T., and Konov, V.I. (2017). Processing constraints resulting from heat accumulation during pulsed and repetitive laser materials processing. Opt. Express *25*, 3966–3979.

39. Lang, V., Roch, T., and Lasagni, A.F. (2016). High-speed surface structuring of polycarbonate using direct laser interference patterning: toward 1 m^2 min^{-1} fabrication speed barrier. Adv. Eng. Mater. *18*, 1342–1348.

40. Chong, T.C., Hong, M.H., and Shi, L.P. (2010). Laser precision engineering: From microfabrication to nanoprocessing. Laser Photonics Rev. *4*, 123–143.

41. Gillner, A., Finger, J., Gretzki, P., Niessen, M., Bartels, T., and Reininghaus, M. (2019). High power laser processing with ultrafast and multi-parallel beams. J. Laser Micro/Nanoengineering *14*, 129–137.

42. Nijhuis, T.A., Kreutzer, M.T., Romijn, A.C.J., Kapteijn, F., and Moulijn, J.A. (2001). Monolithic catalysts as efficient three-phase reactors. Chem. Eng. Sci. *56*, 823–829.

43. Sánchez, O.G., Birdja, Y.Y., Bulut, M., Vaes, J., Breugelmans, T., and Pant, D. (2019). Recent advances in industrial CO_2 electroreduction. Curr. Opin. Green Sustain. Chem. *16*, 47–56.

44. Raciti, D., Livi, K.J., and Wang, C. (2015). Highly dense Cu nanowires for low-overpotential CO_2 reduction. Nano Lett. *15*, 6829–6835.

45. Min, S., Yang, X., Lu, A.-Y., Tseng, C.-C., Hedhili, M.N., Li, L.-J., and Huang, K.-W. (2016). Low overpotential and high current CO_2 reduction with surface reconstructed Cu foam electrodes. Nano Energy *27*, 121–129.

46. Mariano, R.G., McKelvey, K., White, H.S., and Kanan, M.W. (2017). Selective increase in CO_2 electroreduction activity at grain-boundary surface terminations. Science *358*, 1187–1192.

47. Feng, X., Jiang, K., Fan, S., and Kanan, M.W. (2015). Grain-boundary-dependent CO_2 electroreduction activity. J. Am. Chem. Soc. *137*, 4606–4609.

48. Mistry, H., Varela, A.S., Bonifacio, C.S., Zegkinoglou, I., Sinev, I., Choi, Y.-W., Kisslinger, K., Stach, E.A., Yang, J.C., Strasser, P., and Cuenya, B.R. (2016). Highly selective plasma-activated copper catalysts for carbon dioxide reduction to ethylene. Nat. Commun. *7*, 12123, 1-9.

49. Verdaguer-Casadevall, A., Li, C.W., Johansson, T.P., Scott, S.B., McKeown, J.T., Kumar, M., Stephens, I.E.L., Kanan, M.W., and Chorkendorff, I. (2015). Probing the active

surface sites for CO reduction on oxide-derived copper electrocatalysts. J. Am. Chem. Soc. *137*, 9808–9811.

50. Ren, D., Fong, J., and Yeo, B.S. (2018). The effects of currents and potentials on the selectivities of copper toward carbon dioxide electroreduction. Nat. Commun. *9*, 925.

51. Hori, Y., Kikuchi, K., and Suzuki, S. (1985). Production of CO and CH_4 in electrochemical reduction of CO_2 at metal electrodes in aqueous hydrogencarbonate solution. Chem. Lett. *14*, 1695–1698.

52. Kortlever, R., Peters, I., Balemans, C., Kas, R., Kwon, Y., Mul, G., and Koper, M.T.M. (2016). Palladium–gold catalyst for the electrochemical reduction of CO_2 to C_1–C_5 hydrocarbons. Chem. Commun. *52*, 10229–10232.

53. Ren, D., Wong, N.T., Handoko, A.D., Huang, Y., and Yeo, B.S. (2016). Mechanistic insights into the enhanced activity and stability of agglomerated Cu nanocrystals for the electrochemical reduction of carbon dioxide to n-propanol. J. Phys. Chem. Lett. *7*, 20–24.

54. Gupta, N., Gattrell, M., and MacDougall, B. (2006). Calculation for the cathode surface concentrations in the electrochemical reduction of CO_2 in $KHCO_3$ solutions. J. Appl. Electrochem. *36*, 161–172.

55. Singh, M.R., Kwon, Y., Lum, Y., Ager III, J.W., and Bell, A.T. (2016). Hydrolysis of Electrolyte Cations Enhances the Electrochemical Reduction of CO_2 over Ag and Cu. J. Am. Chem. Soc. *138*, 13006–13012.

56. Ooka, H., Figueiredo, M.C., and Koper, M.T.M. (2017). Competition between hydrogen evolution and carbon dioxide reduction on copper electrodes in mildly acidic media. Langmuir *33*, 9307–9313.

57. Schouten, K.J.P., Qin, Z., Gallent, E.P., and Koper, M.T.M. (2012). Two pathways for the formation of ethylene in CO reduction on single-crystal copper electrodes. J. Am. Chem. Soc. *134*, 9864–9867.

58. Cheng, T., Xiao, H., and Goddard, W.A. (2017). Full atomistic reaction mechanism with kinetics for CO reduction on Cu(100) from ab initio molecular dynamics free-energy calculations at 298 K. Proc. Natl. Acad. Sci. U.S.A *114*, 1795-1800.

59. Garza, A.J., Bell, A.T., and Head-Gordon, M. (2018). Mechanism of CO_2 reduction at copper surfaces: pathways to C_2 products. ACS Catal. *8*, 1490–1499.

60. Zhuang, T.-T., Pang, Y., Liang, Z.-Q., Wang, Z., Li, Y., Tan, C.-S., Li, J., Dinh, C.T., De Luna, P., Hsieh, P.-L., Burdyny, T., Li, H.-H., Liu, M., Wang, Y., Li, F., Proppe, A., Johnston, A., Nam, D.-H., Wu, Z.-Y., Zheng, Y.-R., Ip, A.H., Tan, H., Chen, L.-J., Yu, S.-H., Kelley, S.O., Sinton, D., and Sargent, E.H. (2018). Copper nanocavities confine intermediates for efficient electrosynthesis of C_3 alcohol fuels from carbon monoxide. Nat. Catal. *1*, 946–951.

61. Hori, Y., Takahashi, R., Yoshinami, Y., and Murata, A. (1997). Electrochemical reduction of CO at a copper electrode. J. Phys. Chem. B *101*, 7075–7081.

62. Jose, A. (2019). Heading to Distributed Electrocatalytic Conversion of Small Abundant Molecules into Fuels , Chemicals , and Fertilizers 1–20.

63. Galan-mascaros, J.R. (2020). Catalysis Science & Technology dioxide , water and sunlight.

64. Brightman, E., Hinds, G., and O'Malley, R. (2013). In situ measurement of active catalyst surface area in fuel cell stacks. J. Power Sources *242*, 244–254.

65. Bard, A.J., and Faulkner, L.R. (2012). Electrochemical Methods - Fundamentals and Applications. John Wiley & Sons, Inc.

66. Thorson, M.R., Siil, K.I., and Kenis, P.J.A. (2013). Effect of Cations on the Electrochemical Conversion of CO_2 to CO. J. Electrochem. Soc. *160*, F69–F74.

Figure 1. Microfabrication and basic characterization of microstructured electrodes.
A) The ultra-short pulsed (USP) laser beam was guided from the source in open space to a galvo scanner through modifying optics resulting in a focal diameter d_{foc}. Kinematic (XYZ) and optical (UV) axes allowed precise alignment of laser and the copper substrate, whereas galvo mirrors enabled fast circular hatching (d_{hatch}) and distribution of the laser pulses for material removal.

Figure 2. FE vs. potential for a copper foil before (Cu, void symbols) and after (LA-Cu-0, filled symbols) laser ablation.
A) products where Cu and LA-Cu-0 show qualitatively similar trends, B) products where LA-Cu-0 outperforms Cu, highlighted for the case of propanol and ethanol (black arrow: Cu, red arrows: LA-Cu-0). Products detected at trace levels are not included (see **Table S2**).

Figure 3. Selectivity maps vs. applied potential and geometry on microstructured electrodes.
Contour maps showing FE for representative C_1 (formate), C_2 (ethanol), C_3 (propanol) products vs. micro-probe length (L) and potential. They were built upon integration of results obtained for L=0-20-40-60-80-100-130 μm measured at −0.6, −0.8, −1.05, and −1.3 V vs. RHE, as indicated by grey dots in the formate map. All other products are depicted in **Figure S9**. The performance of non-structured laser ablated regions among micro-probes was assimilated to that of Cu-LA-0. (see **Supplemental Experimental Procedures** for details).

Figure 4. Computational modelling under eCO$_2$RR conditions.
A) The concentrations of relevant species in the interior of the micro-probe under analysis (blue) were calculated upon modelling using a finite-element approach in the COMSOL® platform. The modelled electrolyte also comprised the interior of the 8 adjacent micro-probes and the diffusion layer. Modelled phenomena are indicated. B)–E) Calculated evolution of pH and CO_2 concentration along the longitudinal axis (z-axis) for selected lengths and potentials. The z coordinate increases toward the interior and is zero at the base of the micro-probe. Insets show the three-dimensional representation of the simulated CO_2 concentration (at −0.6 V vs. RHE) or pH (at −1.3 V vs. RHE).

Figure 5. Selectivity maps for eCO$_2$RR products vs. chemical environment descriptors.
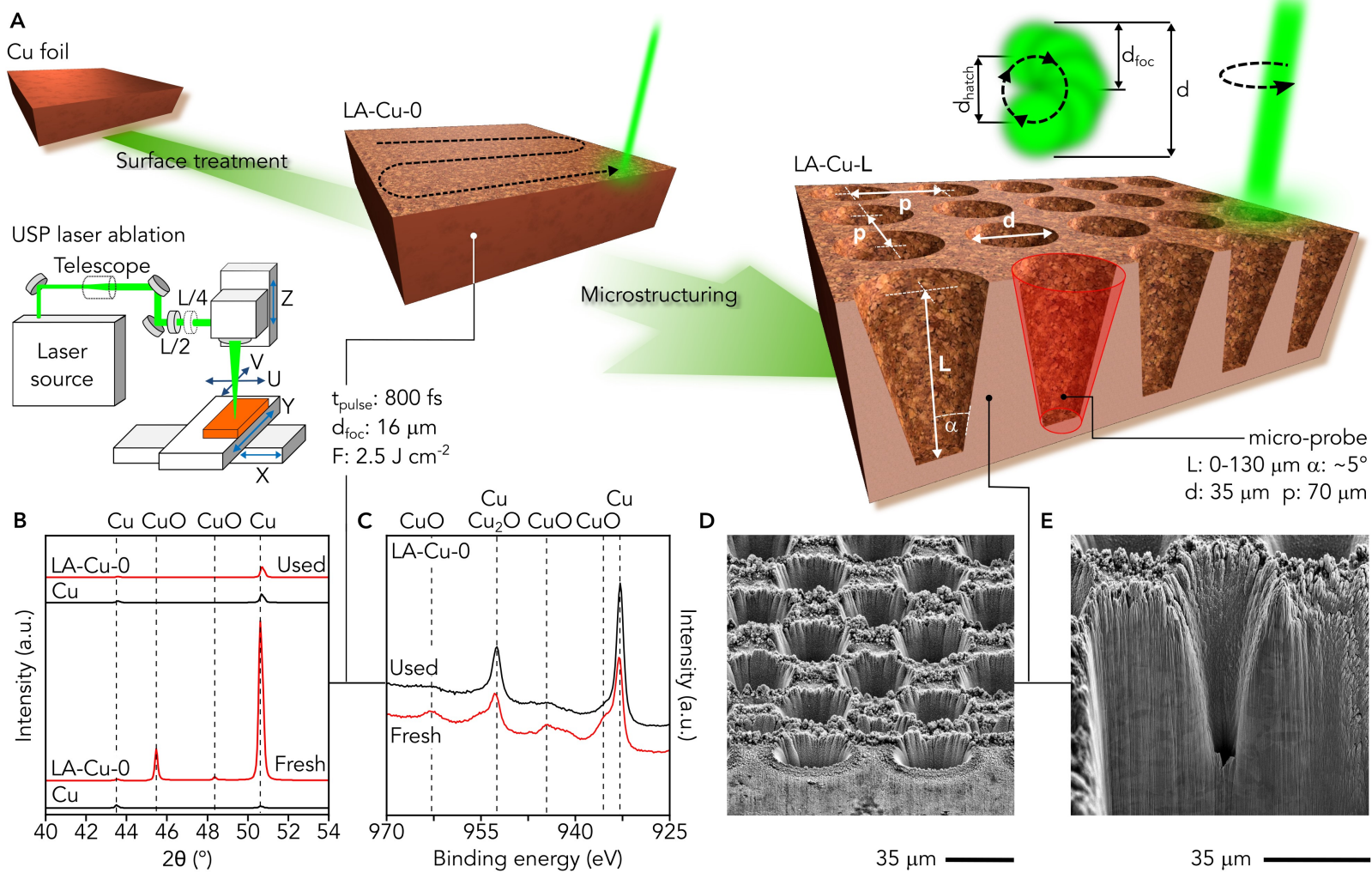Contour maps showing FE versus calculated average pH and CO_2 concentration in the interior of micro-probes. White regions correspond to pH/[CO_2] pairs not allowed by equilibria under reaction conditions
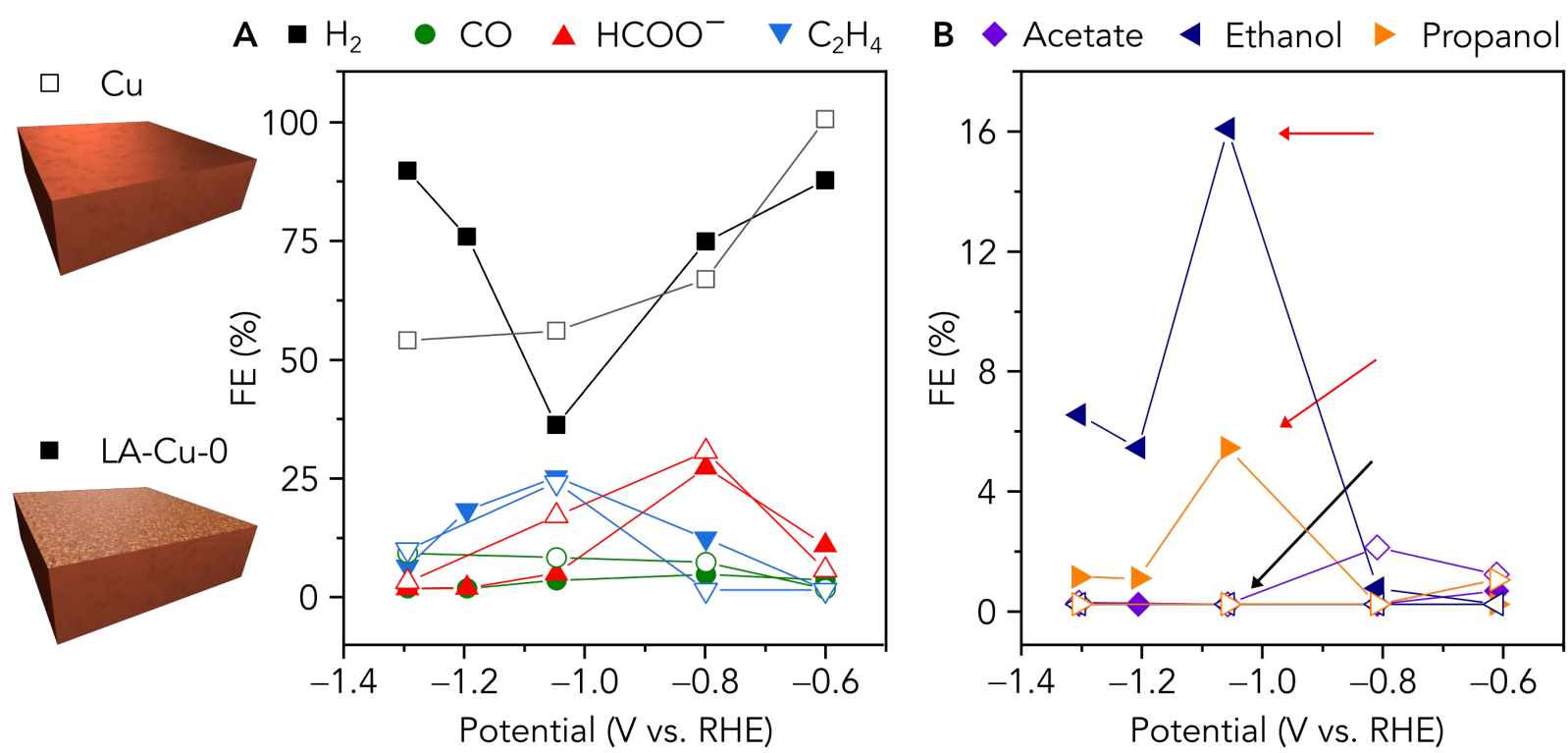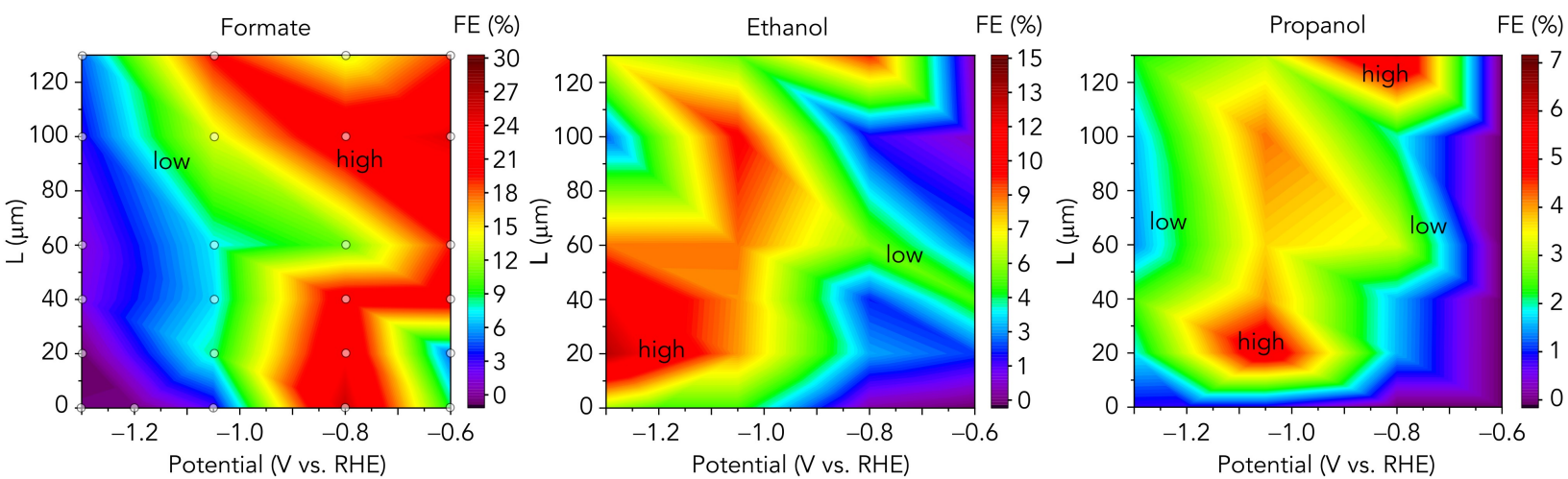
Figure 6. Combined selectivity map.
Contour map showing high FE zones with respect to calculated average pH and CO_2 concentration in the interior of micro-probes upon overlaying and smoothing of maps presented in **Figure 6**. The dots represent local FE maxima. The equivalent map built upon direct overlapping of maps and including the experiments modelled can be found in **Figure S13**.

Figure 7. Effect of enhanced mass transport and electrolyte composition on selectivity.
A) Contour map in **Figure 6** showing the calculated chemical environment for LA-Cu-100 exposed to −1.05 V vs. RHE in 0.1 M KHCO$_3$ (K$^+$), 0.1 M KHCO$_3$ under stirring (K$_s^+$), and 0.1 M CsHCO$_3$ (Cs$^+$). B) representation of the local chemical environment next to the surface and product distribution for the case K$^+$. C, D) similar to B) for the cases of K$_s^+$ and Cs$^+$, respectively, with predicted selectivities obtained from maps in Figure 5 (dashed lines).
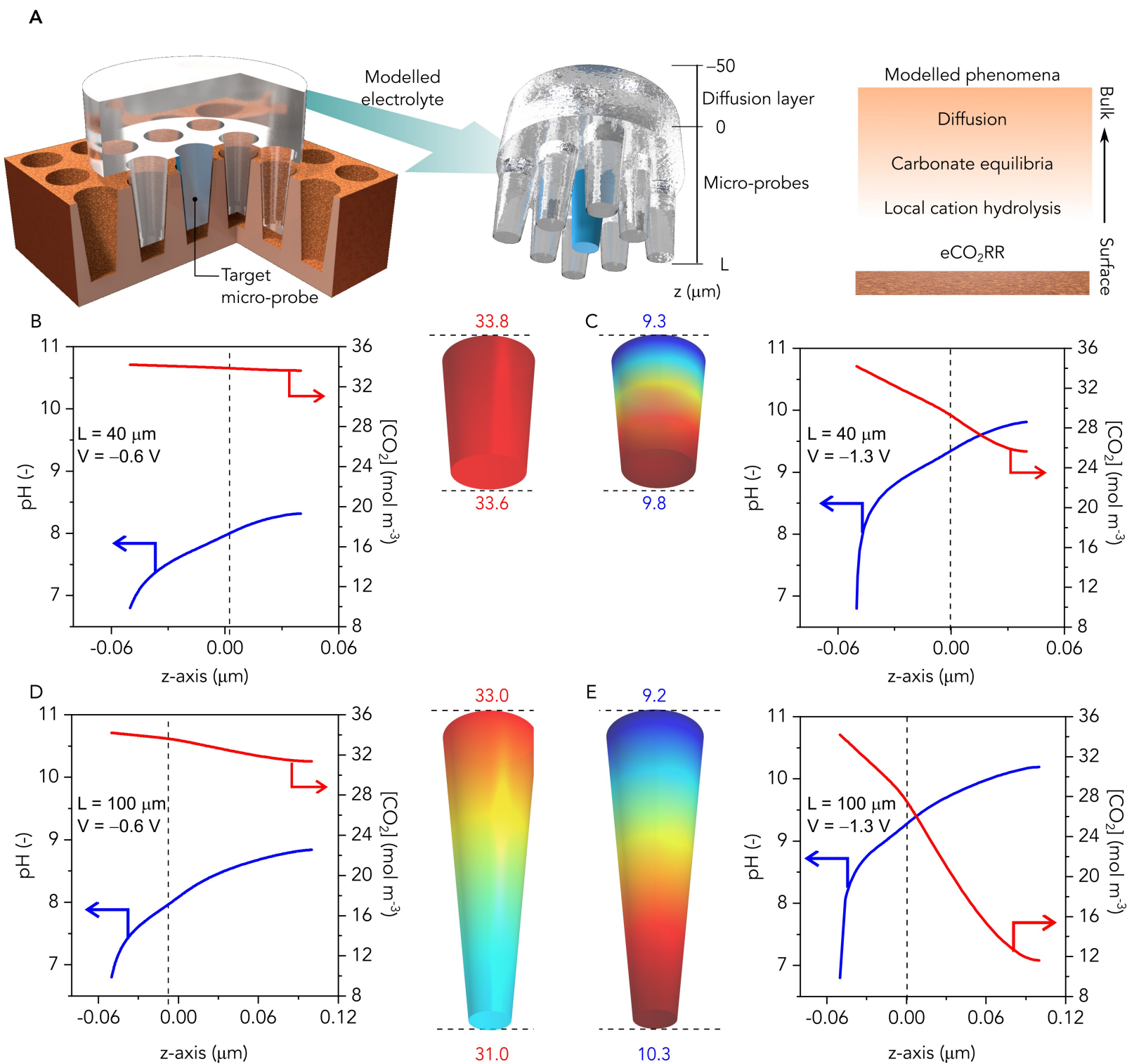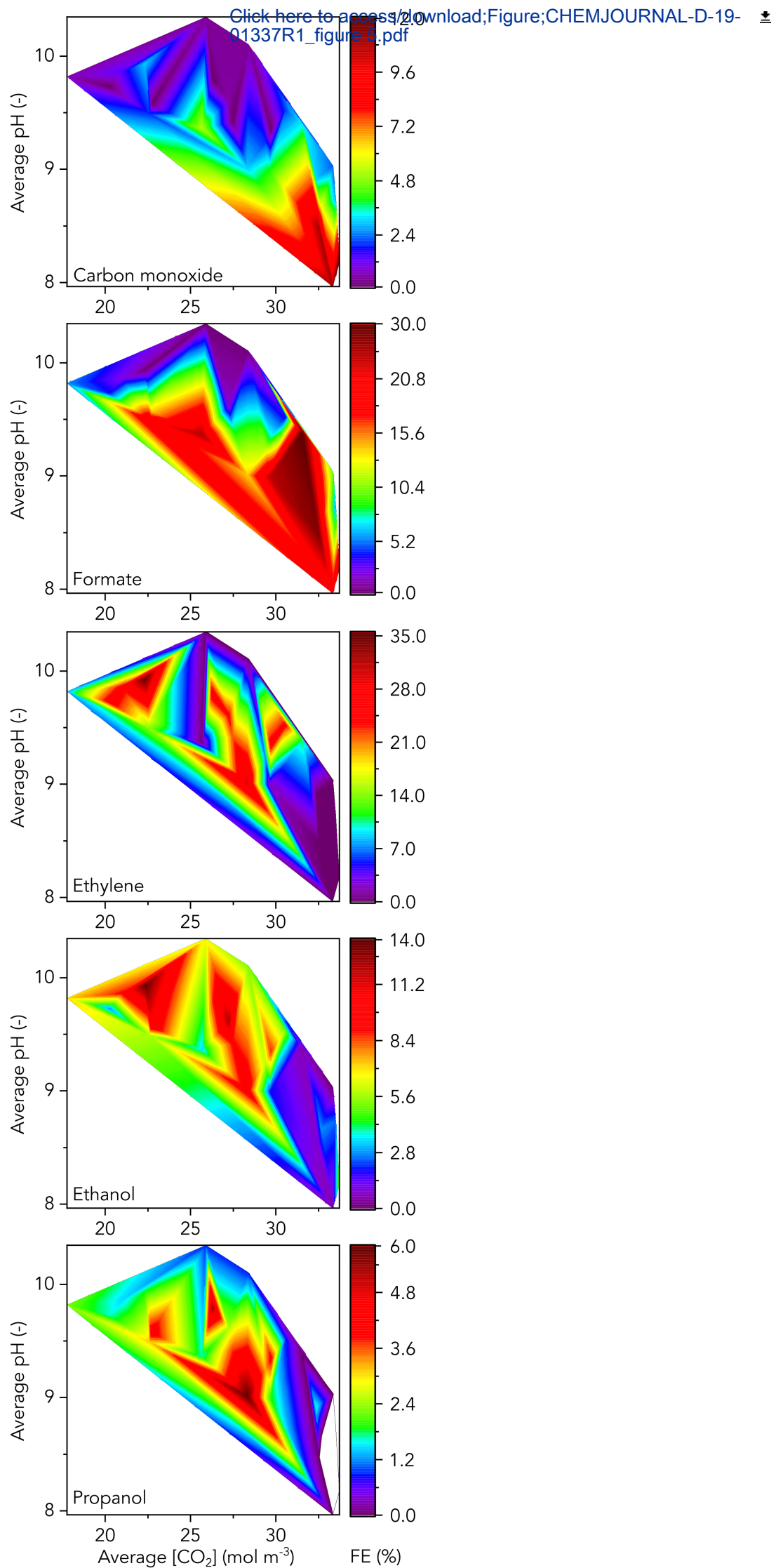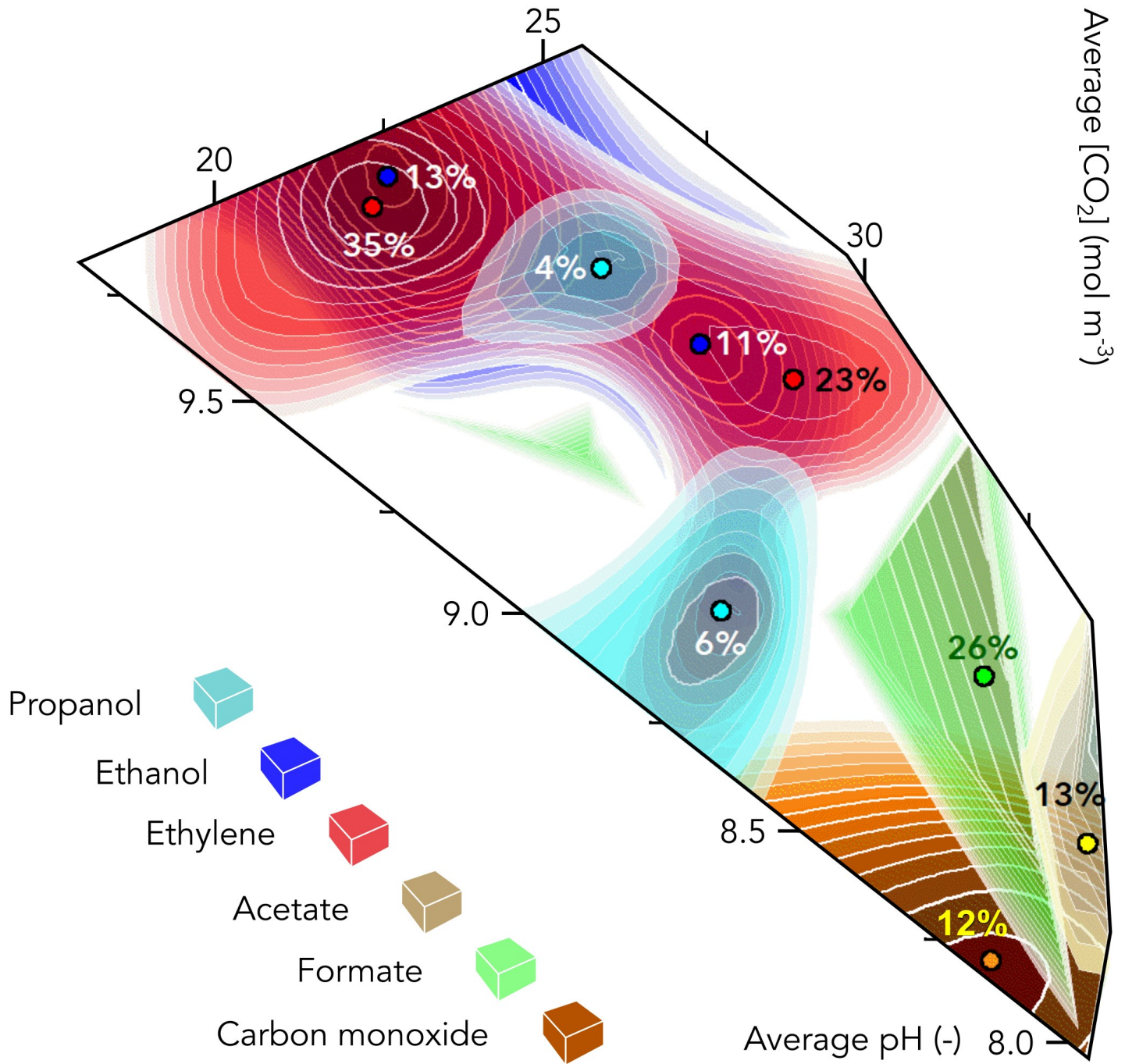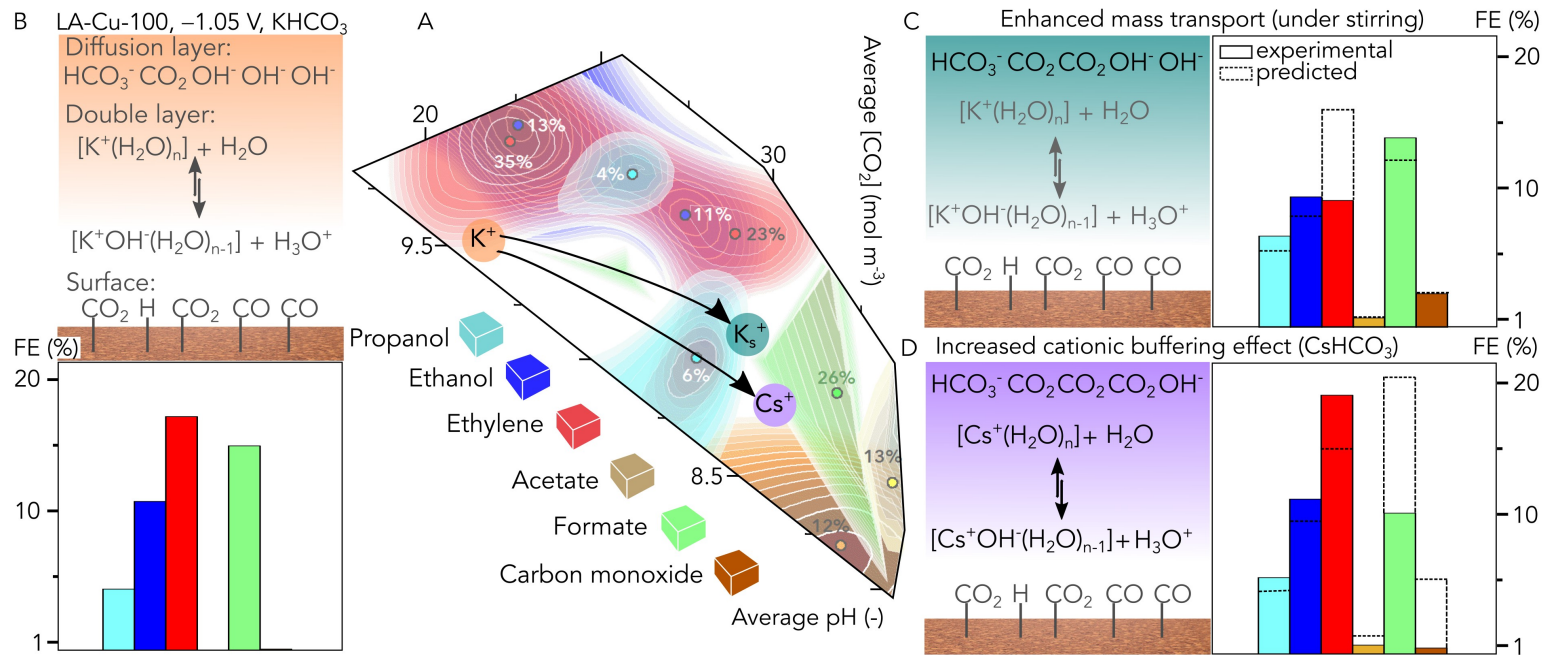
A

Cu foil

Surface treatment

LA-Cu-0

USP laser ablation

Telescope

L/4

Z

L/2

Laser source

V

U

Y

X

t_{pulse}: 800 fs
d_{foc}: 16 μm
F: 2.5 J cm^{-2}

d_{hatch}

d_{foc}

d

LA-Cu-L

p

p

d

L

α

Microstructuring

micro-probe
L: 0-130 μm α: ~5°
d: 35 μm p: 70 μm

B

Cu CuO CuO Cu

LA-Cu-0   Used
Cu

LA-Cu-0   Fresh
Cu

Intensity (a.u.)

40 42 44 46 48 50 52 54
2θ (°)

C

CuO Cu Cu$_2$O CuO Cu CuO

LA-Cu-0

Used

Fresh

Intensity (a.u.)

970   955   940   925
Binding energy (eV)

D

35 μm

E

35 μm

Figure 5

Figure 6

Chem

Supplemental Figures
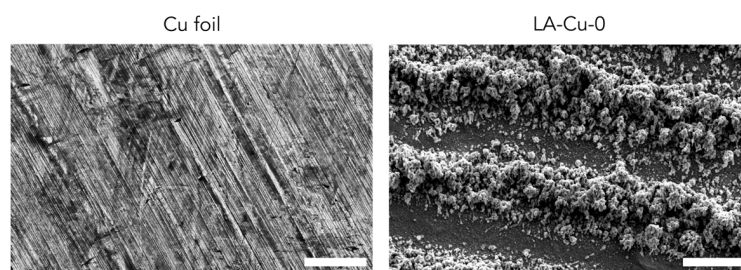

Cu foil   LA-Cu-0

Figure S1. Roughness induced by laser ablation, Related to Figure 1.
SEM micrographs of a pristine Cu foil and after laser ablation, showing the redeposition of ablated Cu following the beam track. Scale bar represents 10 μm.
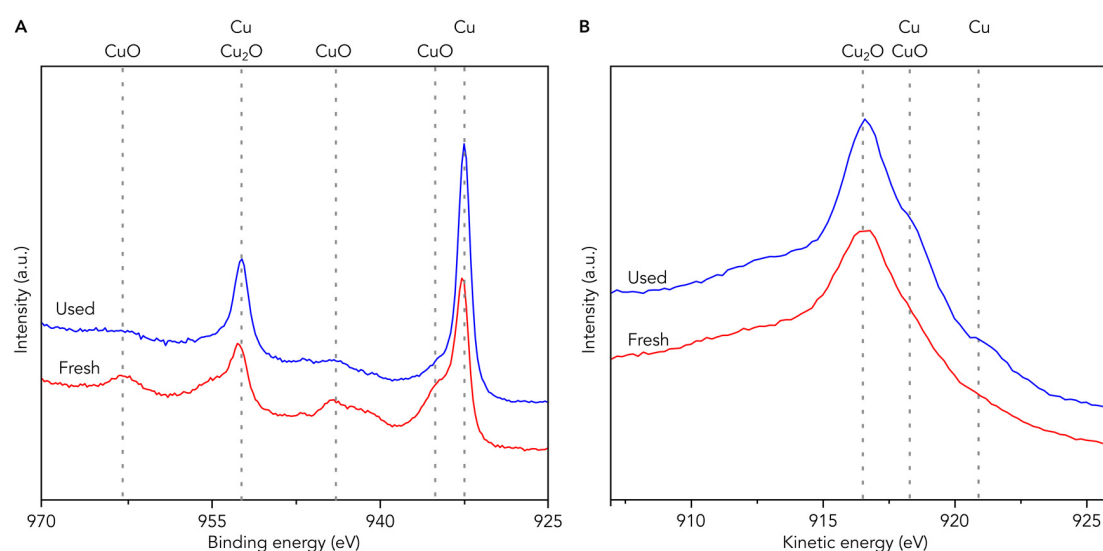

Figure S2. Surface compositional analysis of laser ablated surfaces, Related to Figure 1.
XPS core level and Auger analyses of fresh and used laser ablated copper foils (LA-Cu-0), A) showing the Cu 2p spectra, B) showing the Cu $L_3M_{4.5}M_{4.5}$ spectra. The presence of Cu_2O can be ascribed to the oxidation of Cu upon exposure to air.
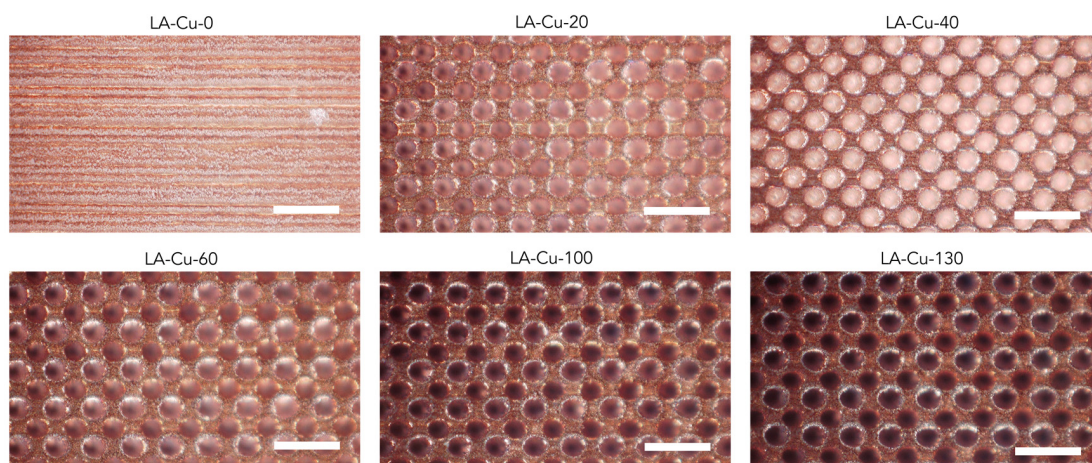
Figure S3. Optical microscopy characterization of microstructured electrodes, Related to Figure 1.

Optical microscopy images (obtained with white light) of representative electrodes for all studied micro-probe lengths. Pitch: 70 µm, diameter: 35 µm, length: 0-130 µm. Scale bars represent 100 µm.
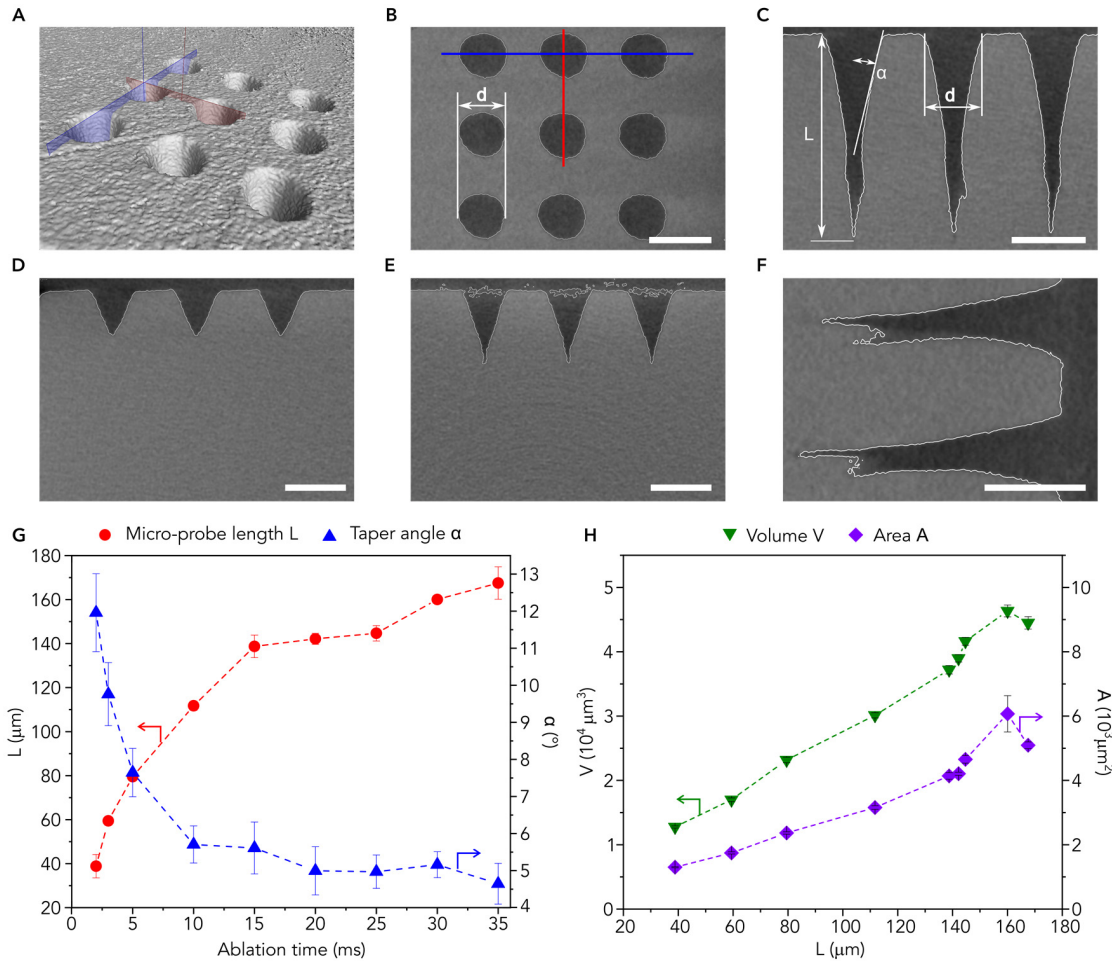
Figure S4. Geometrical characterization of micro-probes, Related to Figure 1.

Microcomputed tomography study on a set of 9 micro-probes per laser parameter used for the manufacturing, A) and B) show the reconstructed volume with two perpendicular planes aligned to the center of adjacent micro-probes. This enables the determination of main geometrical parameters defining the volume, depicted in C). By increasing the number of laser pulses per hole, the length was increased, as observed in D) and E). The deformation in F) is caused by multiple reflections of the laser beam. The variations of the length and taper angle with the time exposed to the laser beam (ablation time) are shown in G). The volume and the area linearly correlate with the length, as shown in H). Scale bars represent 50 μm.
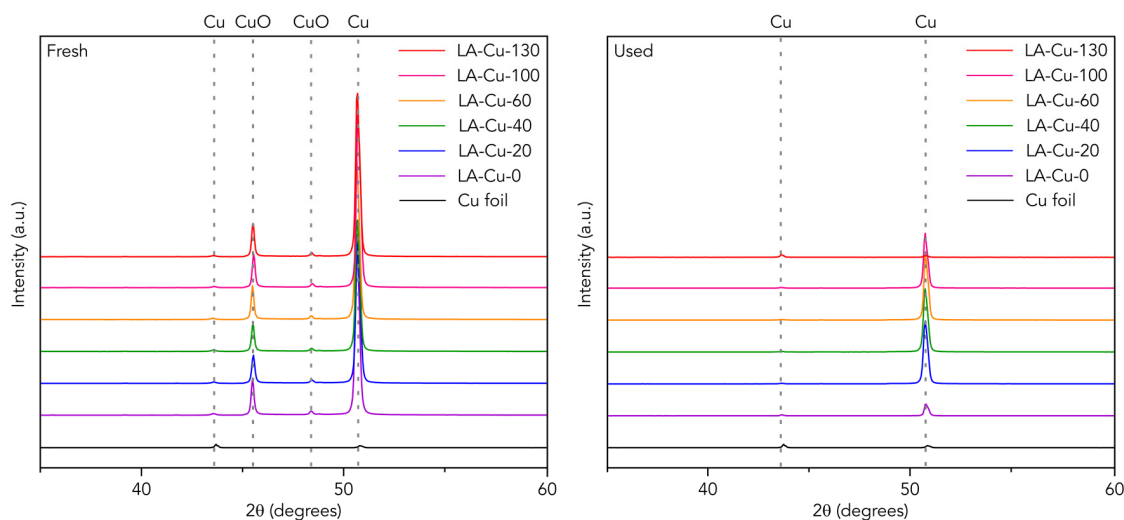
Figure S5. Crystalline structure and phase identification of microstructured electrodes, Related to Figure 1 and Figure 3.
XRD patterns before and after electrolysis. The position of the main reflections for relevant phases is indicated.
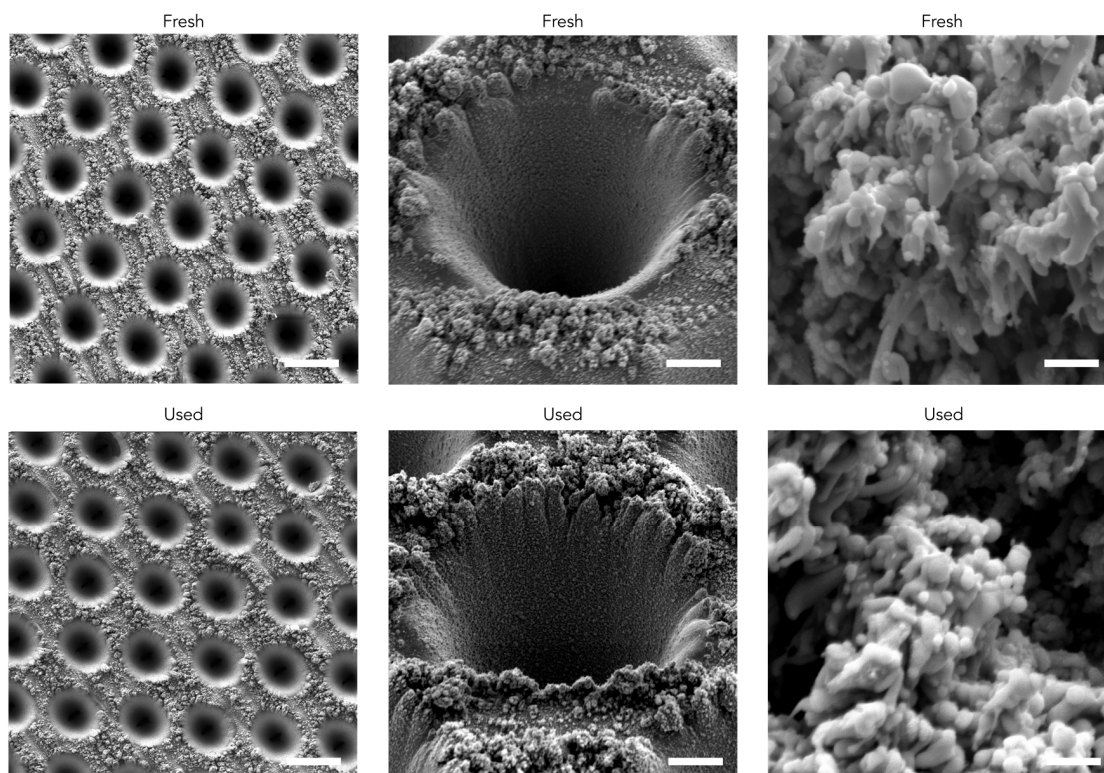

Figure S6. SEM analysis of microstructured electrodes, Related to Figure 3.
SEM micrographs of Cu-LA-60 before and after electrocatalytic tests. Scale bar represents 50 μm (left), 5 μm (center), 1 μm (right).
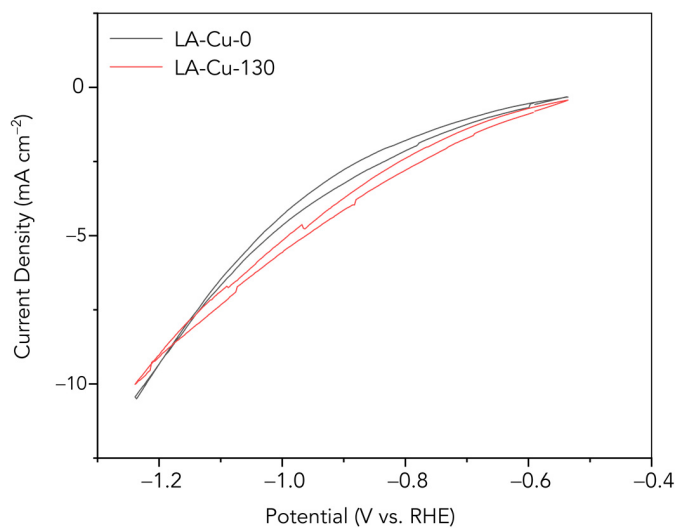
Figure S7. Cyclic voltammetries for LA-Cu-0 and LA-Cu-130 after exposure to reaction conditions, Related to Figure 3.

Cyclic voltammetries in the reaction medium (0.1 M KHCO$_3$ saturated with CO$_2$) of a copper foil after laser ablation pretreatment (LA-Cu-0) and subsequent microstructuring (LA-Cu-130).
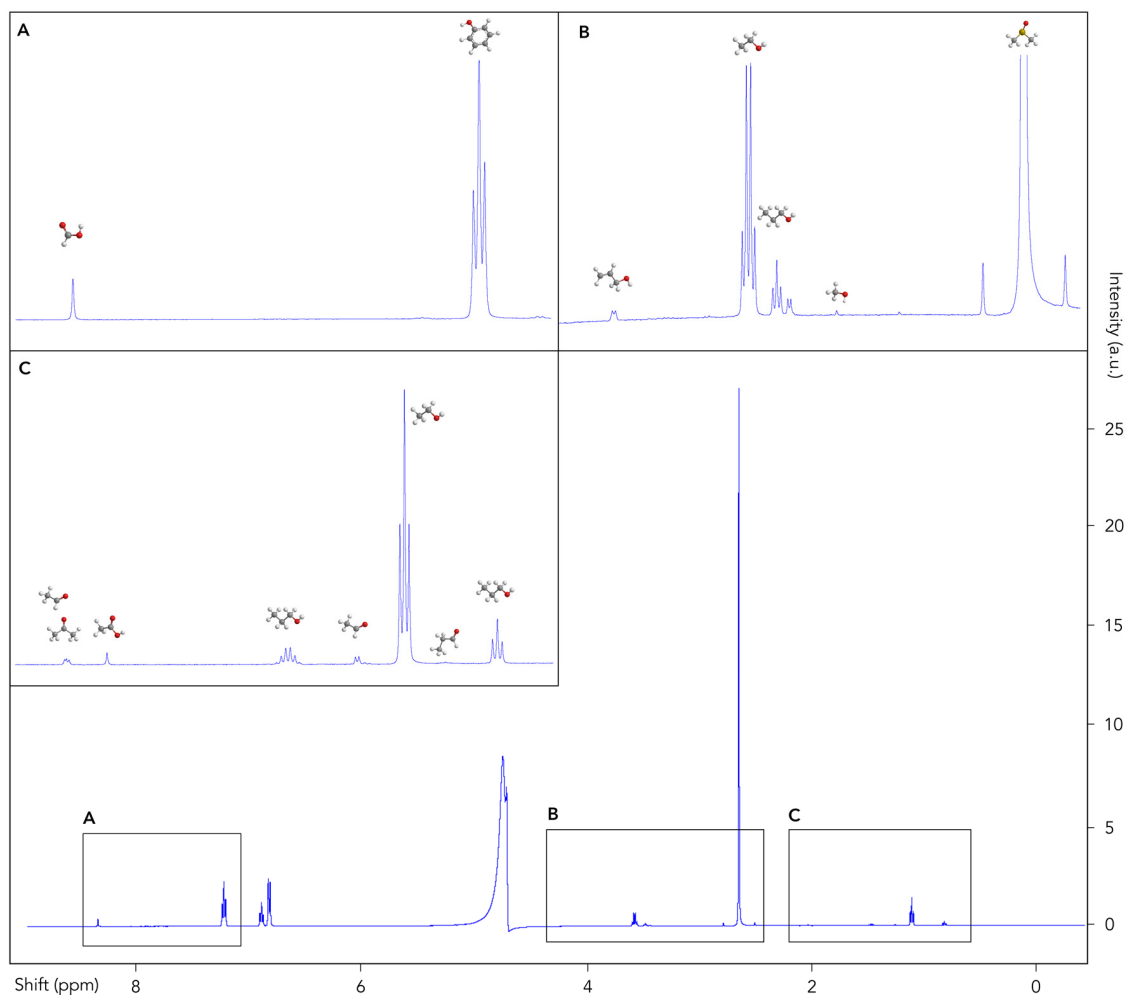
Figure S8. Identification and quantification of liquid products, Related to Figure 2 and Figure 3.

Representative ^{1}H-NMR spectrum obtained from analysis of the catholyte after electrolysis. Case shown: LA-Cu-0 exposed to −1.05 V vs. RHE. A) Formate and phenol (internal standard), B) allyl alcohol, ethanol, propanol, methanol, dimethyl sulfoxide (internal standard), C) acetaldehyde with acetone, acetate, propanol, acetaldehyde, ethanol, propionaldehyde, and propanol. Spectra were obtained with a Bruker III 500 MHz. Color code: oxygen (red), carbon (grey), hydrogen (white).
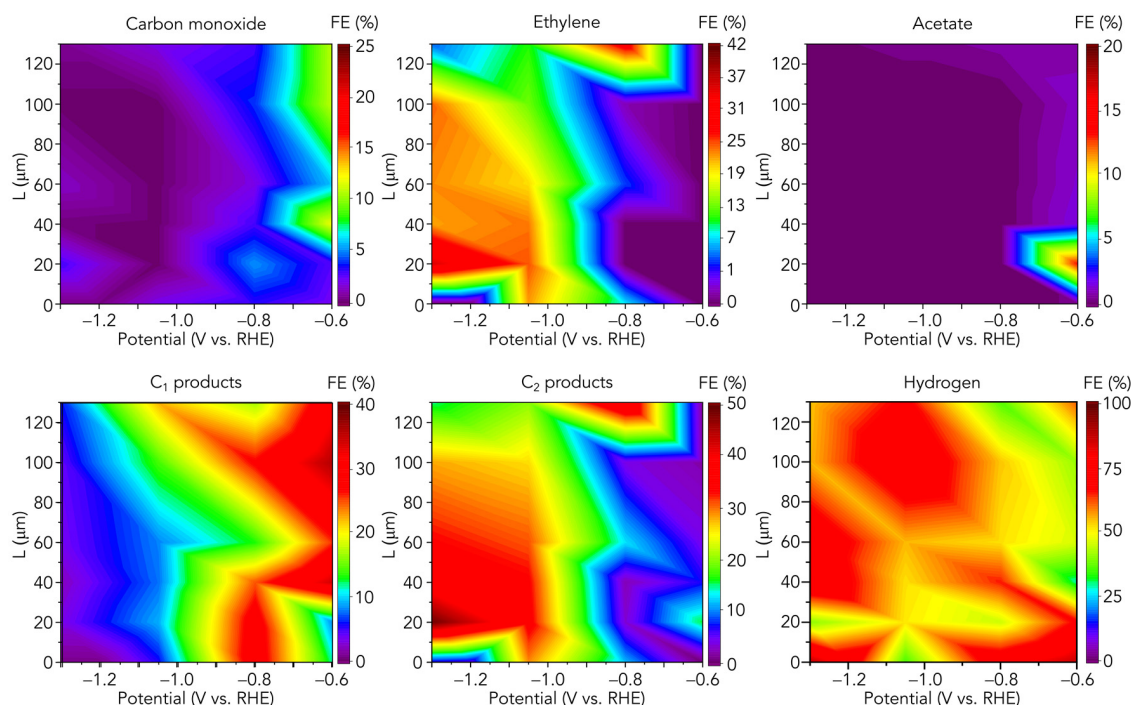
Figure S9. Selectivity vs. potential and geometry on microstructured electrodes, Related to Figure 3.

Contour maps showing Faradaic efficiency (FE) vs. micro-probe length (L) and potential as subsidiary results to Figure 3 (top row). Aggregated maps showing the sum of FE for C_1 and C_2 products and the contour map for the parasitic H_2 formation are shown in the bottom row.
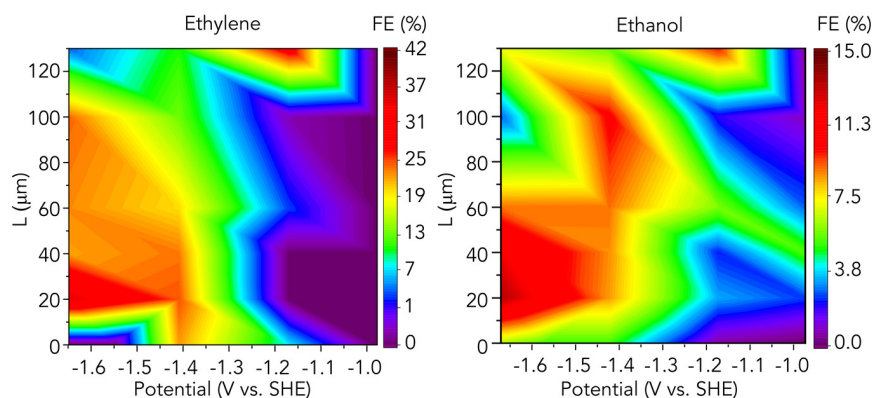

Figure S10. Selectivity toward ethylene and ethanol vs. standard hydrogen electrode (SHE) potential and geometry on microstructured electrodes, Related to Figure 3.

Contour maps showing Faradaic efficiency (FE) vs. micro-probe length (L) and potential vs. SHE as subsidiary results to ethylene in Figure S9 and ethanol in Figure 3.
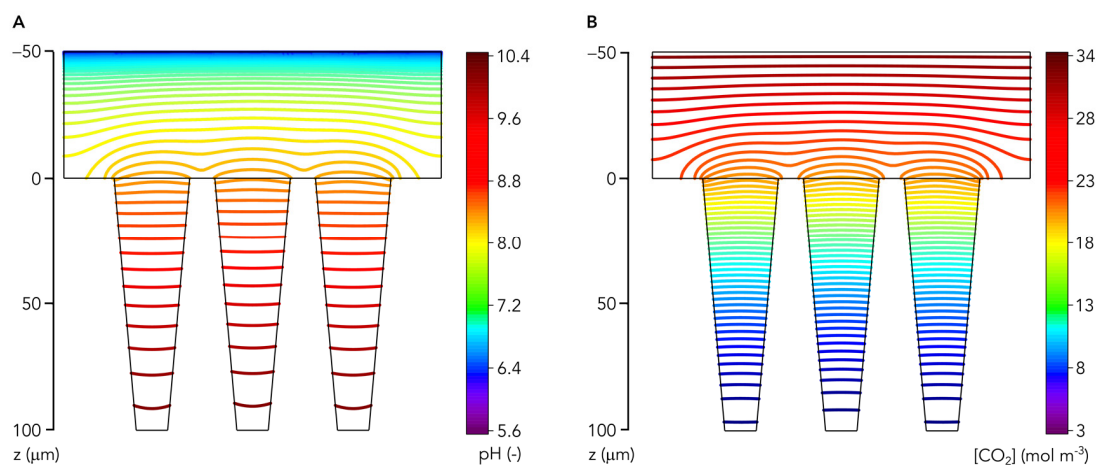
Figure S11. Simulated 2D isocontours under eCO₂RR conditions, Related to Figure 4.
Representative case (LA-Cu-100 exposed to −1.3 V vs. RHE) showing isocontour lines obtained from simulations for A) pH and B) CO_2 concentration over a cross-section comprising the axes of three adjacent probes. The almost perpendicular shape of isocontour lines in the interior of the micro-probes with respect to the longitudinal axis allows considering these two 3D variables as 1D, only dependent on the z-coordinate, without loss of generality.

Figure S12. Simulated CO₂ flux under eCO₂RR conditions, Related to Figure 4.
Distribution of the CO_2 flux over LA-Cu-40 and LA-Cu-100 operated at low (−0.6 V) and high (−1.3 V) potentials (see Figure S13 for the corresponding OH^- simulations). The CO_2 flux is described by its value (isosurfaces) and direction (arrows) and develops from the bulk toward the interior. Differences betw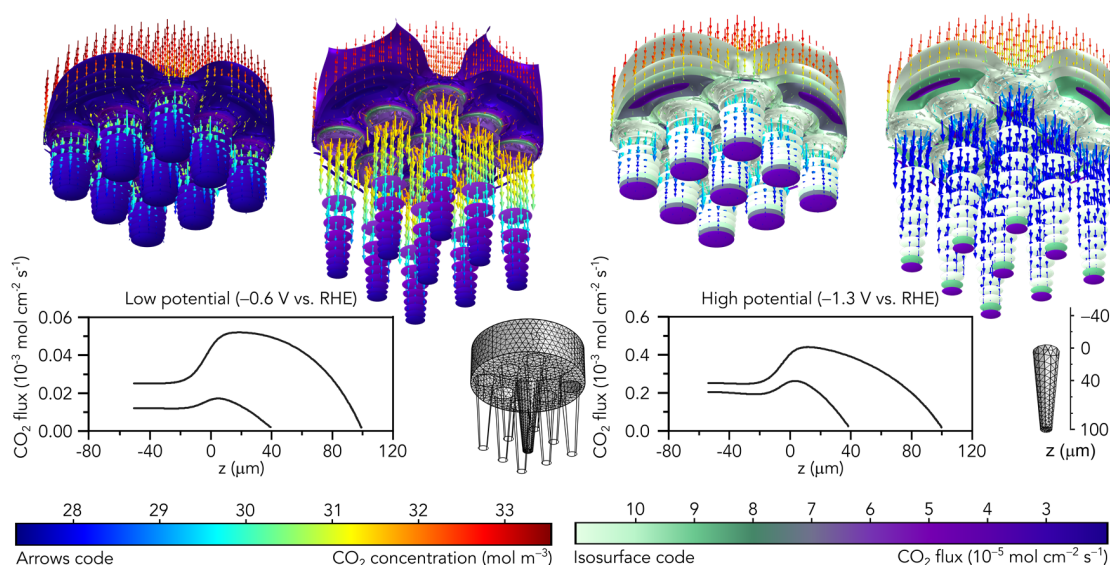een low (left) and high (right) potentials are readily noticeable. The electrodes operated at low potentials display negligible flux of CO_2 irrespective of L, since the overall CO_2 concentration is close to the bulk one due to the low reaction rate (Table S6). The OH^- flux is also modest and follows the opposite direction, i.e., toward the exterior of the micro-probes, as shown in Figure S13. On the other hand, higher potentials present values of CO_2 flux one order of magnitude larger, thus suggesting a more heterogeneous environment less prone to fine control. Nonetheless, the 2D evolutions of the CO_2 flux along the z-axis show a common behavior defined by an initial increase from z = o until a maximum and a further decline toward zero at z = L (boundary condition). Notably, the maximum flux is closely controlled by the potential and its position by L (Figure S14).
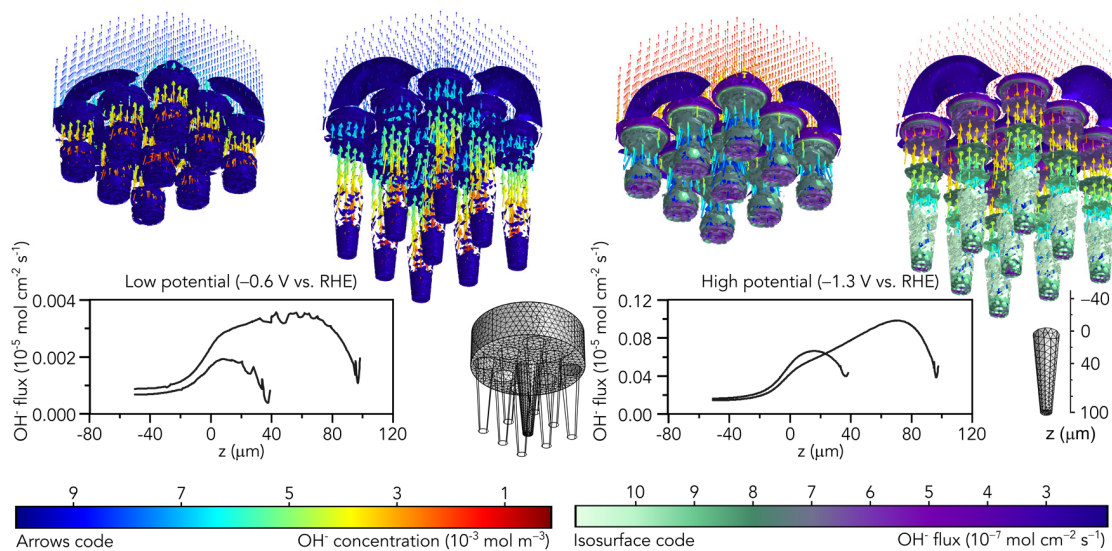
Figure S13. Simulated OH⁻ flux, Related to Figure 4.

Isosurfaces displaying the distribution of the OH⁻ flux. Arrows show the flux direction and are colored according to the local concentration of OH⁻, whereas their length is proportional to the total flux value. Insets represent the evolution along the z-axis. Cases shown: LA-Cu-40 and LA-Cu-100 at low (−0.6 V vs. RHE, left) and high potentials (−1.3 V vs. RHE, right).
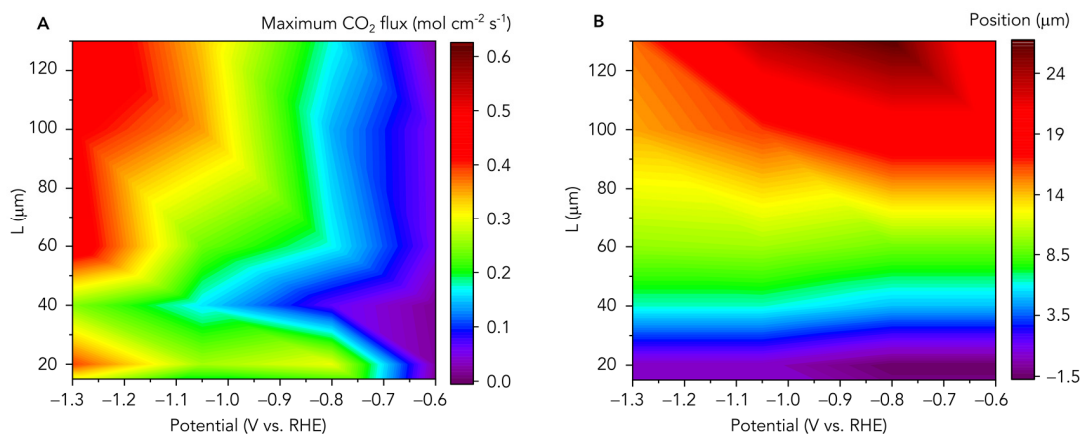
Figure S14. Dependence of the maximum CO₂ flux inside the micro-probes with the applied potential and geometry, Related to Figure 4.
Contour maps showing A) the maximum CO_2 flux and B) its position in the z-axis obtained in the simulations, represented vs. micro-probe length and potential.
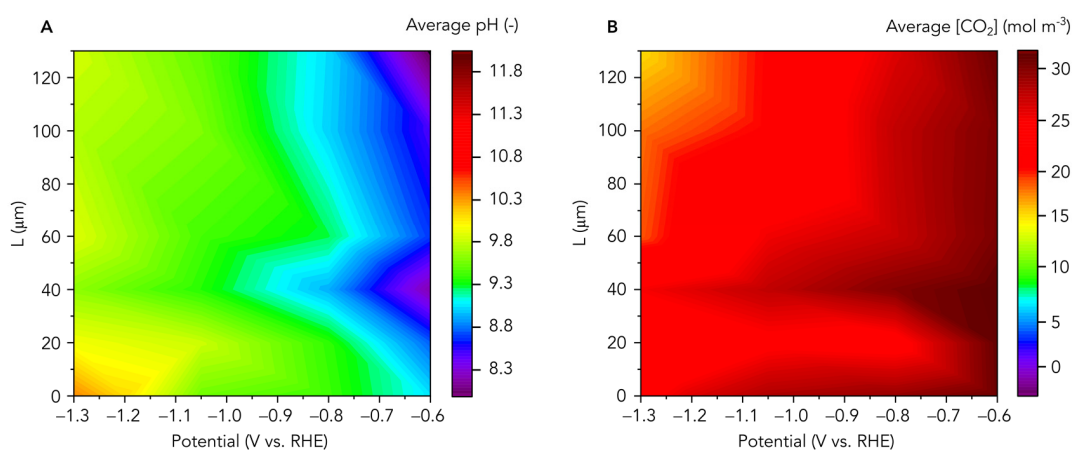
Figure S15. Dependence of the chemical environment descriptors in the micro-probes with the applied potential and geometry, Related to Figure 4.
Contour maps displaying average A) pH and B) CO_2 concentration vs. micro-probe length and applied potential.
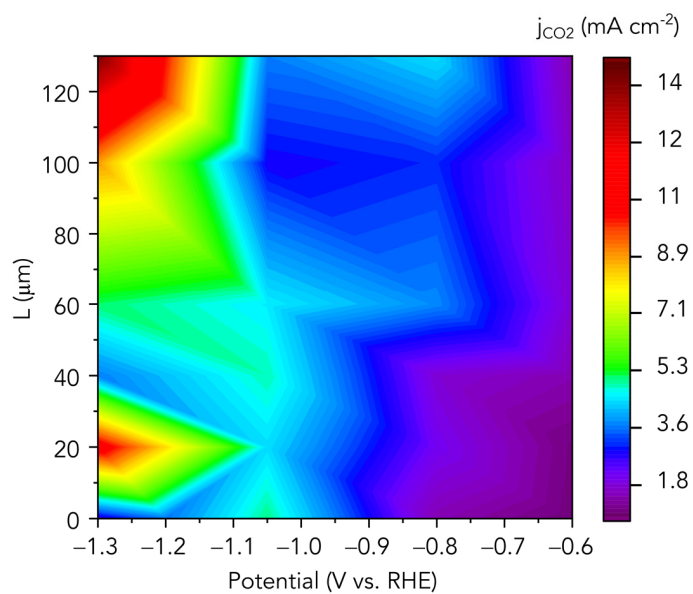
Figure S16. CO₂ reduction current vs. potential and geometry on microstructured electrodes, Related to Figure 3.
Contour map showing the sum of measured partial current densities for carbon products vs. micro-probe length (L) and potential.
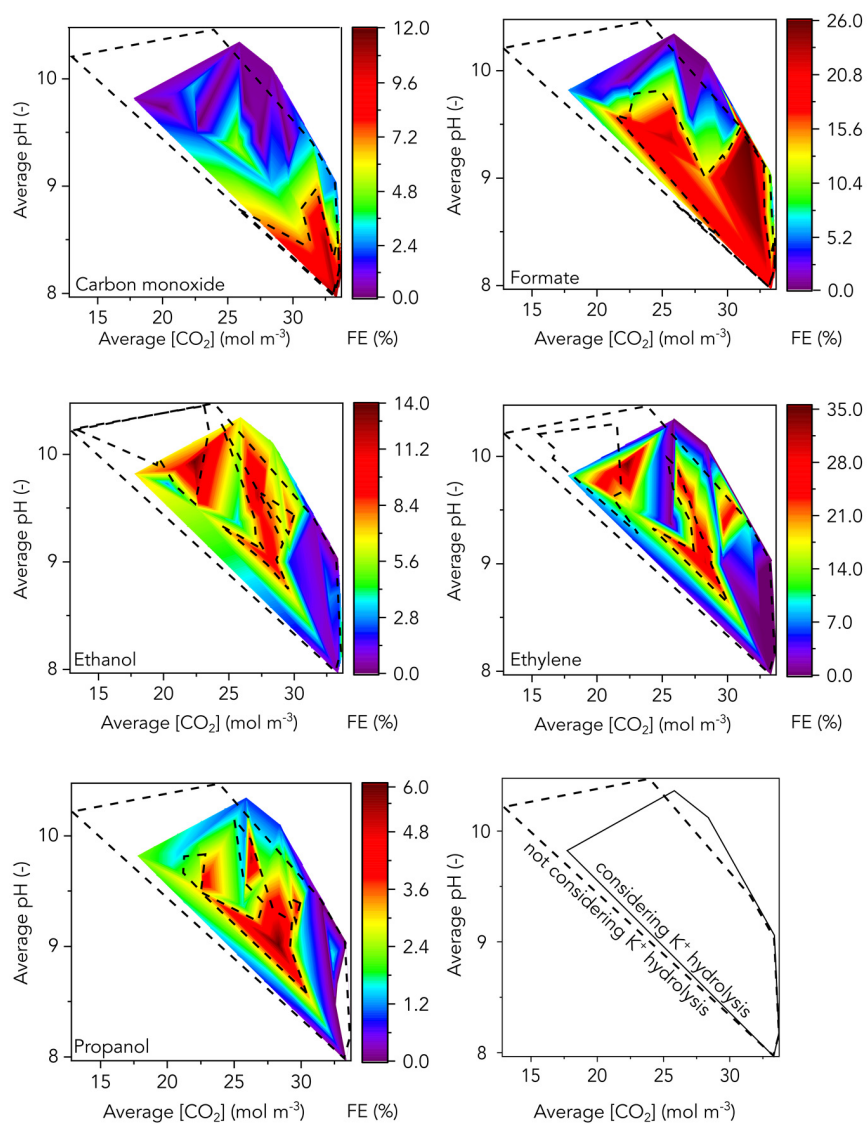
Figure S17. Effect of cation hydrolysis in the local chemical environment, Related to Figure 5.

Comparison between selectivity maps obtained through simulations including (solid lines) and not including (dashed lines) the effect of hydrolysis of K^+ in the vicinity of the catalyst surface. For the sake of simplicity, only the contour of the maps and high selectivity regions are shown for the simulations disregarding hydrolysis.
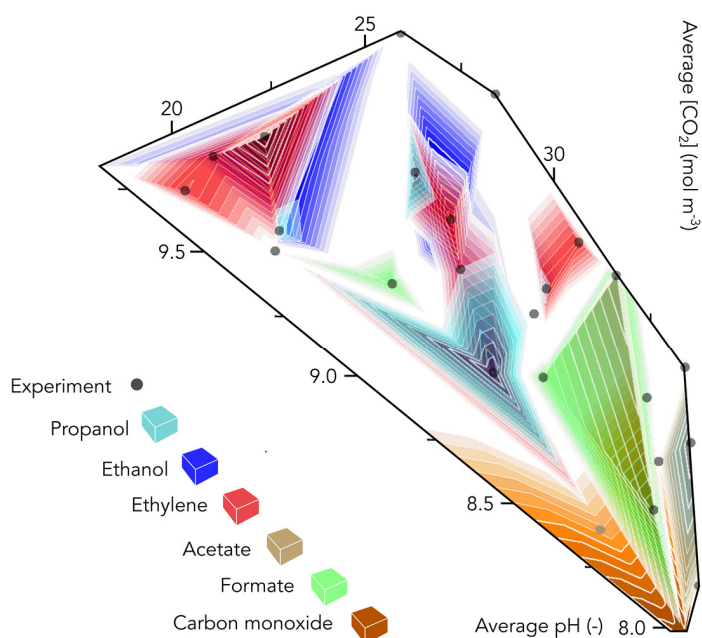
Figure S18. Combined selectivity map, Related to Figure 6.
Contour map showing regions with high Faradaic efficiency for relevant products with respect to calculated average pH and CO_2 concentration in the interior of the micro-probes upon overlaying of maps presented in Figure 5. Grey dots indicate modelled experiments (see Figure 3).
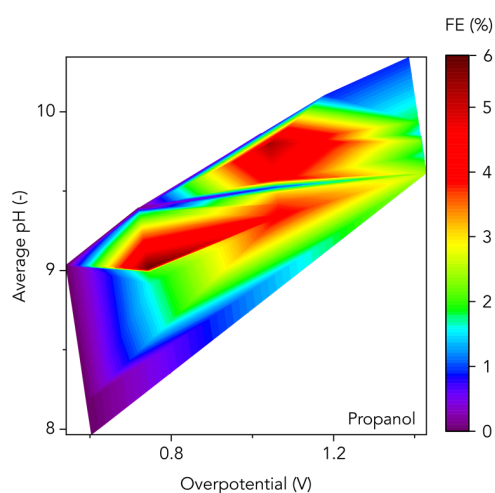
Figure S19. Faradaic efficiency vs. calculated overpotential and average pH for the case of propanol, Related to Figure 5.
Contour map showing regions where propanol is favored. Overpotentials were calculated based on applied potentials and the Nernst equation after considering correction by the simulated local concentrations of H^+ and CO_2.
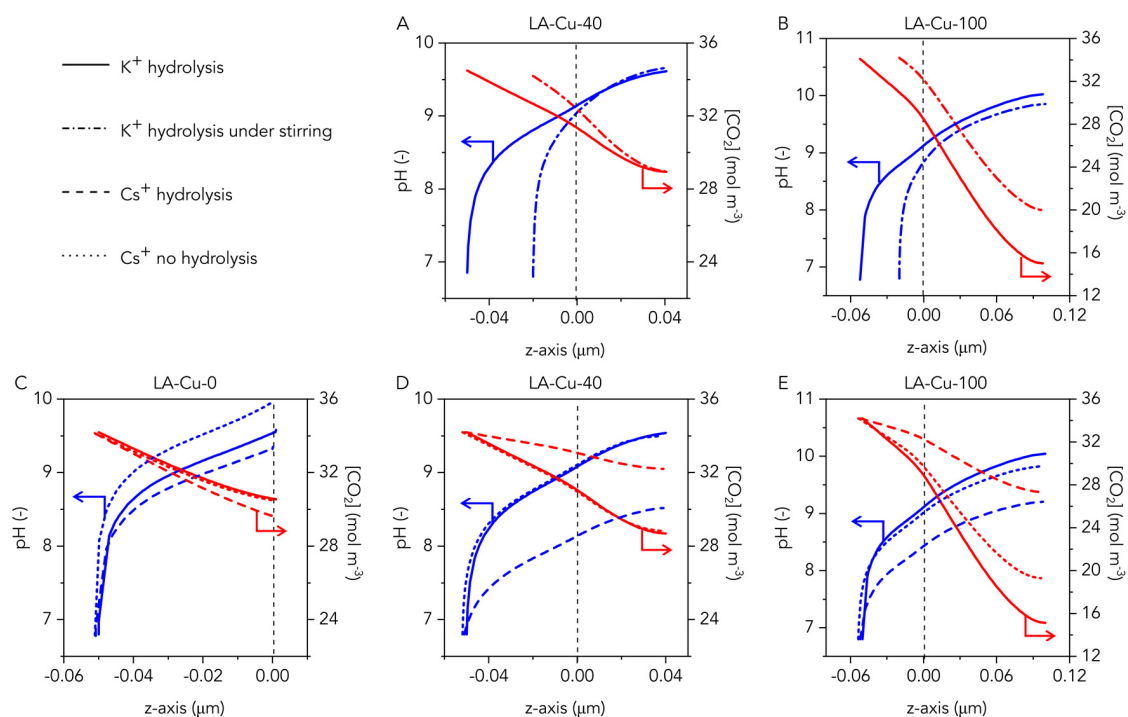
Figure S20. Effect on the chemical environment in the micro-probes of enhanced mass transport and the nature of the electrolyte, Related to Figure 7.
Evolution along the axis of micro-probes of pH and CO_2 concentration for representative electrodes. A) and B) display the effect of stirring, whereas C-E) display the effect of using $CsHCO_3$ instead of $KHCO_3$.

Supplemental Tables

Table S1. Double layer capacitances and ratios related to Cu foil of microstructured electrodes, Related to Figures 2, 3, and 4.

Electrode	Capacitance ($\mu F\ cm^{-2}$)	Ratio
Cu foil	27.63	1.00
LA-Cu-0	84.86	3.02
LA-Cu-20	173.27	6.40
LA-Cu-40	768.92	27.80
LA-Cu-60	864.11	32.12
LA-Cu-100	1309.71	43.37
LA-Cu-130	1636.76	59.21

Table S2. Faradaic efficiencies for secondary products at different potentials on microstructured electrodes, Related to Figure 3 and S6.

| Potential (V vs. RHE)	Micro-probe length (μm)	CH_4 (%)	CH_3OH (%)	C_2H_4O (%)	$C_2H_6O_2$ (%)	C_3H_6O (%) Acetone	Propional-dehyde	Allyl alcohol
−0.6	Cu foil	0	0	0	1	0	0	0
−0.6	LA-Cu-0	0	0	0	0	0	0	0
−0.6	LA-Cu-20	0	0.129	0.386	2.573	1.287	0	0
−0.6	LA-Cu-40	0	0.095	0.284	0	0	0.190	0
−0.6	LA-Cu-60	0	0.082	0.082	0.082	0.041	0.164	0.082
−0.6	LA-Cu-100	0	0.058	0.404	0	0	0.346	0
−0.6	LA-Cu-130	0	0	0	0	0	0	0
−0.8	Cu foil	0	0	0	1.917	0	0	0
−0.8	LA-Cu-0	0	0.014	0	0	0	0	0
−0.8	LA-Cu-20	0	0.034	0.103	0	0.855	0.274	0.308
−0.8	LA-Cu-40	0	0.056	0.111	0	0.028	0.223	0.167
−0.8	LA-Cu-60	0	0.044	0.074	0.088	0	0.118	0.324
−0.8	LA-Cu-100	0	0	0	0	0	0	0
−0.8	LA-Cu-130	0	0.047	0.095	0.111	0	0.190	0.605
−1.05	Cu foil	0	0.116	0	0	0	0.225	0.859
−1.05	LA-Cu-0	0	0.087	0	0	0	0	1.711
−1.05	LA-Cu-20	0	0.108	0.108	1.294	0	0.647	1.213
−1.05	LA-Cu-40	0	0.030	0.100	0.450	0	0.200	0.599
−1.05	LA-Cu-60	0	0.029	0.775	0.097	0	0.581	0.775
−1.05	LA-Cu-100	0	0.093	0.037	1.773	0	0.187	0.630
−1.05	LA-Cu-130	0	0	0.092	0	0	0.184	0.415
−1.2	LA-Cu-0	0	0.026	0	0	0	0	0.210
−1.3	Cu foil	0	0.051	0	0.059	0	0.041	0.314
−1.3	LA-Cu-0	0	0.051	0.051	0	0	0	0.230
−1.3	LA-Cu-20	3	0.057	0.057	0.137	0	0.106	0.456
−1.3	LA-Cu-40	1.5	0.049	0	0	0	0	0.294
−1.3	LA-Cu-60	1.4	0.049	0.063	0.102	0	0.068	0.322
−1.3	LA-Cu-100	0	0.013	0.022	0.026	0	0.087	0.167
−1.3	LA-Cu-130	1.6	0.095	0	0.190	0.009	0	0

Table S3. Faradaic efficiencies for major products at different potentials in 0.1 M KHCO$_3$ on microstructured electrodes, Related to Figure 3 and S6.

Potential (V vs. RHE)	Micro-probe length (μm)	H$_2$ (%)	CO (%)	HCO$_2^-$ (%)	C$_2$H$_4$ (%)	C$_2$H$_3$O$_2^-$ (%)	C$_2$H$_5$OH (%)	C$_3$H$_7$OH (%)
−0.6	Cu foil	100	0.3	4.3	2.0	0.8	0.0	0.0
−0.6	LA-Cu-0	87	2.2	9.5	0.0	0.4	0.0	0.0
−0.6	LA-Cu-20	67	2.7	5.5	0.1	13.3	2.5	0.0
−0.6	LA-Cu-40	29	12.0	22.3	0.1	1.6	5.4	0.0
−0.6	LA-Cu-60	46	6.0	19.7	0.1	1.4	2.8	0.0
−0.6	LA-Cu-100	41	11.0	24.9	0.0	1.2	0.9	0.0
−0.6	LA-Cu-130	61	10.9	19.3	0.0	0.9	0.5	0.0
−0.8	Cu foil	66	6.0	29.4	1.9	0.0	0.0	0.0
−0.8	LA-Cu-0	74	3.3	26.0	11.0	0.0	0.6	0.0
−0.8	LA-Cu-20	45	5.2	23.4	0.1	0.0	3.3	1.6
−0.8	LA-Cu-40	65	3.0	21.8	0.1	0.0	2.3	1.6
−0.8	LA-Cu-60	52	2.0	11.2	7.0	0.0	5.9	3.2
−0.8	LA-Cu-100	54	4.0	23.0	2.0	0.0	2.0	2.0
−0.8	LA-Cu-130	36	3.0	14.0	30.0	0.8	9.8	5.8
−1.05	Cu foil	55	6.9	15.7	0.0	0.0	2.3	1.4
−1.05	LA-Cu-0	35	2.1	3.5	24.0	0.0	5.3	0.9
		63[b]	1.2[b]	20.9[b]	1.8[b]	0.5[b]	6.7[b]	4.9[b]
−1.05	LA-Cu-20	51	0.1	9.0	26.0	0.0	8.6	5.3
−1.05	LA-Cu-40	52	0.1	7.6	25.0	0.0	8.7	4.0
		62[a]	2.5[a]	12.3[a]	19.8[a]	0.6[a]	7.2[a]	5.2[a]
		55[b]	0.0[b]	10.4[b]	20.0[b]	0.5[b]	10.8[b]	4.8[b]
−1.05	LA-Cu-60	55	0.1	8.0	22.0	0.0	9.0	3.7
−1.05	LA-Cu-100	77	0.1	14.0	16.0	0.0	10.2	4.2
		55[a]	2.3[a]	13.0[a]	8.7[a]	0.7[a]	8.9[a]	6.3[a]
		58[b]	0.4[b]	9.6[b]	17.7[b]	0.6[b]	10.6[b]	5.2[b]
−1.05	LA-Cu-130	68	2.0	20.2	14.0	0.5	5.7	3.1
−1.2	LA-Cu-0	75	0.4	0.5	0.0	0.0	5.3	0.9
−1.3	Cu foil	53	7.9	1.7	0.1	0.0	6.4	0.6
−1.3	LA-Cu-0	89	0.4	0.4	0.0	0.0	6.4	0.9
−1.3	LA-Cu-20	40	3.0	0.2	35.4	0.0	13.4	1.9
−1.3	LA-Cu-40	58	0.3	2.6	6.2	0.1	7.5	1.3
		60[a]	0.8[a]	3.3[a]	32.9[a]	0.3[a]	11.1[a]	3.8[a]
−1.3	LA-Cu-60	75	1.4	2.2	24.5	0.0	9.0	1.4
−1.3	LA-Cu-100	55	0.1	4.1	25.4	0.0	2.7	1.6
		49[a]	0.7[a]	3.4[a]	21.1[a]	0.3[a]	14.2[a]	3.9[a]
−1.3	LA-Cu-130	54	0.6	5.5	7.8	0.2	7.1	2.2

a) Under stirring
b) In 0.1 M CsHCO$_3$

Table S4. Total current densities related to the geometrical area at different cathodic potentials in 0.1 M KHCO$_3$ over microstructured electrodes, Related to Figure 3.

Micro-probe length (μm)	Current density (mA cm^{-2})			
	−0.6 V vs. RHE	−0.8 V vs. RHE	−1.05 V vs. RHE	−1.3 V vs. RHE
LA-Cu-0[a]	−1.17	−2.71	−7.39	−17.88
LA-Cu-20	−0.70	−2.58	−8.26	−18.77
LA-Cu-40	−0.96	−3.09	−9.64	−18.01
LA-Cu-60	−1.96	−6.80	−9.35	−19.50
LA-Cu-100	−1.51	−6.52	−9.99	−20.27
LA-Cu-130	−1.70	−6.33	−9.92	−33.41

a) LA-Cu-0 was also tested at −1.2 V vs. RHE; −12.37 mA cm^{-2}

Table S5. Reactions considered in the model and corresponding stoichiometric parameters: n_k and m_k are the stoichiometric coefficients for CO_2 and OH^-, respectively, and z_k the number of electrons transferred per molecule of product, Related to Figure 4.

Reaction	n_k	m_k	z_k
$2H_2O + 2e^- \rightarrow H_2 + 2OH^-$	-	2	2
$CO_2 + H_2O + 2e^- \rightarrow CO + 2OH^-$	1	2	2
$CO_2 + H_2O + 2e^- \rightarrow HCOO^- + OH^-$	1	1	2
$CO_2 + 6H_2O + 8e^- \rightarrow CH_4 + 8OH^-$	1	8	8
$2CO_2 + 9H_2O + 12e^- \rightarrow C_2H_5OH + 12OH^-$	2	12	12
$2CO_2 + 8H_2O + 12e^- \rightarrow C_2H_4 + 12OH^-$	2	12	12
$2CO_2 + 10H_2O + 14e^- \rightarrow C_2H_6 + 14OH^-$	2	14	14
$3CO_2 + 13H_2O + 18e^- \rightarrow C_3H_7OH + 18OH^-$	3	18	18

Table S6. Bulk equilibria reactions at 25 °C considered in the model and corresponding rate constants,[1] Related to Figure 4.

Reaction	$k_{forward}$ (M^{-1} s^{-1})	$k_{reverse}$ (s^{-1})
$CO_2(aq) + OH^- \leftrightarrow HCO_3^-$	5.93 10^3	1.34 10^{-4}
$HCO_3^- + OH^- \leftrightarrow CO_3^{2-} + H_2O$	1 10^9 (assumed)	2.5 10^4

Table S7. Diffusion coefficients[2] at infinite dilution at 25 °C and bulk concentrations in CO_2-saturated 0.1 M $KHCO_3$, Related to Figure 4.

Species	D^0 (m^2 s^{-1})	C_{bulk} (mol m^{-3})
CO_2	1.91×10^{-9}	34.2
HCO_3^-	9.23×10^{-10}	99.7
CO_3^{2-}	1.19×10^{-9}	29.4
OH^-	5.27×10^{-9}	6.3×10^{-2}

Table S8. Cell voltages at different cathodic potentials in 0.1 M $KHCO_3$ over microstructured electrodes, Related to Figure 5.

Micro-probe length (μm)	Cell voltage (V)			
	−0.6 V vs. RHE	−0.8 V vs. RHE	−1.05 V vs. RHE	−1.3 V vs. RHE
LA-Cu-0[a]	3.24	4	5.4	7.4
LA-Cu-20	3.3	4.21	5.7	8.4
LA-Cu-40	3.14	3.76	5.22	7.88
LA-Cu-60	3.35	4.37	5.6	7.8
LA-Cu-100	3.5	4.1	5.15	7.2
LA-Cu-130	3.45	4.5	5.75	8.92

a) LA-Cu-0 was also tested at −1.2 V vs. RHE; 5.97 V

Table S9. Values obtained from simulations for the concentration of CO$_2$ and pH averaged over the z-axis, and the maximum flux of CO$_2$ and its position, Related to Figure 5, 6, and 7.

Potential (V vs. RHE)	Micro-probe length (µm)	Averaged z-axis		Maximum CO$_2$ flux	
		[CO$_2$] (mol m^{-3})	pH (-)	Value (mol m^{-2} s^{-1})	z (µm)
−0.6	LA-Cu-0	33.362	9.0315	n.a.	n.a.
−0.6	LA-Cu-20	33.509	8.7357	0.0216	-1.5
−0.6	LA-Cu-40	33.725	8.1758	0.0172	5
−0.6	LA-Cu-60	32.665	8.6625	0.0541	9
−0.6	LA-Cu-100	32.537	8.4721	0.0519	19
−0.6	LA-Cu-130	33.332	7.9652	0.02495	17
−0.8	LA-Cu-0	31.552	9.3945	n.a.	n.a.
−0.8	LA-Cu-20	25.677	9.3632	0.296	-1.5
−0.8	LA-Cu-40	32.362	8.9124	0.0653	5
−0.8	LA-Cu-60	29.395	9.2443	0.1685	9
−0.8	LA-Cu-100	29.641	8.9924	0.142	19
−0.8	LA-Cu-130	28.332	9.0093	0.1708	26
−1.05	LA-Cu-0	30.569	9.5249	n.a.	n.a.
		29.733[b]	9.3226[b]	n.a.	n.a.
		26.081[c]	9.9221[c]	n.a.	n.a.
−1.05	LA-Cu-20	26.275	9.7995	0.261	0
−1.05	LA-Cu-40	29.719	9.3429	0.1607	6.3
		31.841[a]	9.2123[a]	0.1447[a]	7[a]
		32.597[b]	8.3501[b]	n.a.	n.a.
		29.821[c]	9.3276[c]	0.1565[c]	5.5[c]
−1.05	LA-Cu-60	27.468	9.4184	0.2358	10
−1.05	LA-Cu-100	22.714	9.5703	0.354	16
		29.062[a]	9.1631[a]	0.213[a]	22[a]
		30.133[b]	8.8079[b]	n.a.	n.a.
		25.293[c]	9.3917[c]	0.275[c]	17[c]
−1.05	LA-Cu-130	22.611	9.4905	0.3363	23
−1.2	LA-Cu-0	28.381	10.105	n.a.	n.a.
−1.3	LA-Cu-0	25.9	10.345	n.a.	n.a.
−1.3	LA-Cu-20	22.335	9.9382	0.39	0
−1.3	LA-Cu-40	27.219	9.6134	0.2463	6.3
		30.469[a]	9.4137[a]	0.2277[a]	6.5[a]
−1.3	LA-Cu-60	20.983	9.8611	0.451	9.7
−1.3	LA-Cu-100	20.243	9.7271	0.424	14
		26.696[a]	9.3993[a]	0.3113[a]	18[a]
−1.3	LA-Cu-130	17.755	9.8185	0.475	15

a) Under stirring
b) In 0.1 M CsHCO$_3$ with Cs$^+$ hydrolysis
c) In 0.1 M CsHCO$_3$ without Cs$^+$ hydrolysis

Supplemental Experimental Procedures

Microstructuring

Copper foils (oxygen-free 2.0040 - Cu OF >3N, 0.3 mm, 20 mm × 20 mm) were processed using ultrashort pulsed (USP) laser ablation[3] to generate a regular distribution of cavities (denoted as micro-probes) with controlled geometry over 2.25 cm^2. These micro-probes showed a slight conical shape with the following dimensions; 70 μm pitch, 35 μm diameter, and 0-130 μm length (Figure 1). Throughout this study, an USP Amphos laser served as source, where the fundamental beam is frequency doubled to 515 nm reaching 800 fs pulse duration and increasing the ablation efficiency of copper. The focal laser beam diameter was set to 16 μm diameter by adjusting the Galilean telescope and using a 160 mm telecentric f-theta objective lens. The laser beam was moved with the galvo scanner orthogonally over the specimen surface layer-by-layer to reach a certain depth. Prior to the micro-probe manufacturing, two layers of the copper foil were removed, resulting in a rougher surface (LA-Cu-0) composed of copper oxide (15 mm x 15 mm), see Figure 1 and S1. The laser beam was steered with 5 μm distance leading to overlap at 500 mm s^{-1} speed, 400 kHz repetition rate, and 2 W average power over the specimen.[4] The second layer was rotated by 90° to mitigate overlapping laser lines while removing about 2 μm of material within 8 min. Subsequently, the micro-probes were laser-machined by a circular movement of the beam with the introduced strategy in Figure 1. This circle hatch was repeated for a certain time between 1 ms and 10 ms at an energy density of 2.5 J cm^{-2}, well above the threshold of ablation for copper, with a surface speed of 500 μm s^{-1}. All relative movements of the laser beam to the substrates were carried out with the galvo scanner, allowing a positioning speed between the probes of 2 m s^{-1}. The micro-probes with length of 20 μm were produced from 4 layers and by increasing the time (and thus the amount of layers), the length was controlled. The micro-probes are aligned with a pitch of 70 μm and a second arrangement of micro-probes shifted half a pitch to generate a denser pattern. This led to ca. 92000 micro-probes with a controlled volume generated in less than two hours depending on desired length. The laser machining time per micro-probe was set to [1, 2, 3, 5, 10] ms to fabricate lengths of [20, 40, 60, 100, 130] μm on top of the initially removed 2 μm of material.

Electrochemical measurements

The electrocatalytic tests over microstructured electrodes were conducted on a custom-made gastight flow-cell consisting of two compartments separated by a Selemion AMV membrane with a continuous gas-flow under a three-electrode configuration. The cell was mounted with a GDL carbon paper acting as the counter electrode (Sigracet 39BC, SGL Carbon) and 2.25 cm^2 exposed microfabricated electrode which were both replaced after every measurement, and a leak-free Ag/AgCl reference electrode (3 M KCl, model LF-1, Innovative Instruments). The cathodic and anodic compartments contained 8 and 7.8 cm^3 of 0.1 M KHCO$_3$, respectively. A steady CO$_2$ flow of 20 cm^3 min^{-1} was bubbled through separately into each compartment, which were saturated with CO$_2$ for at least 20 minutes prior to the start of electrolyses, resulting in pH 6.7. The electrochemical measurements were conducted by an Autolab PGSTAT302N potentiostat at room temperature, with all potential values reported versus the reversible hydrogen electrode (RHE) scale. The 50-min eCO$_2$RR experiments were carried out with the R compensation function set at 85% of the uncompensated resistance R$_u$, determined prior to the electrolysis by electrochemical impedance spectroscopy (EIS) measurements at high frequency. R$_u$ was calculated every 7.5 min during each experiment and used to continuously correct the applied overpotential. Following this procedure, the applied potentials were within 10 mV of the target potential of the electrolysis.

Product analysis

The gaseous products were analyzed every 15 min by an on-line Gas-Chromatography (GC) through a connection between the cathodic compartment and the sample loop of an SRI 8610C gas chromatograph (Multi-Gas #3 configuration). The compounds were separated using argon carrier gas under a pressure of 2.3 bar by a combination of HayeSep-D and Molecular Sieve 13X packed columns. The Faradaic efficiency (FE_i) for each gas-phase product during the electrolysis was obtained by dividing the partial current density (j_i) by the total current density at the sampling time (i_t), see (equation 1). The given value corresponds to the average over the entire electrolysis.

$$FE_{i,gas} = \frac{j_i}{i_t} \times 100 \tag{1}$$

Liquid products formed during CO_2 electrolysis were quantified by ^{1}H-NMR. Following the reaction, catholyte and anolyte samples (0.7 cm^3) were each mixed with D_2O (0.05 cm^3) containing phenol (50 mM) and dimethyl sulfoxide (50 mM) as internal standards. 1D ^{1}H-NMR spectra with water suppression of the sample were recorded on a Bruker Avance III HD 500 MHz mounted with a 5 mm BBO Prodigy (at room temperature). One pulse experiment was pre-saturated on the water resonance with a $\pi/2$ pulse of 12 μs (at a power of 15.9 W, accounting for -12.1 dB) and a recycle delay of 5 s (with preset power of 9.2×10^{-5} W accounting for 40.38 dB) was implemented while coadding 256 scans per experiment. These settings resulted in a high signal-to-noise ratio and an analysis time of ca. 35 minutes per sample. The calculation of the Faradaic efficiency for liquid-phase products is given by (equation 2),

$$FE_{i,liquid} = \frac{V_e C_i nF}{q_{tot}} \times 100 \tag{2}$$

Where V_e is the volume of the electrolyte, C_i is the molar concentration of the product in the electrolyte, and q_{tot} is the total charge passed during the electrolysis.

Catalyst characterization

X-ray diffraction (XRD) patterns of the electrodes were obtained in a PANalytical X'Pert PRO MPD diffractometer with Bragg-Brentano geometry using Ni-filtered CuKα radiation (λ = 0.1541 nm). The instrument was operated at 30 mA and 10 kV and the patterns were recorded in the 5-70° 2θ range with an angular step size of 0.05° and an integration time of 5 s per step. X-ray photoelectron spectroscopy (XPS) analysis was carried out with a PHI Quantum 2000 spectrometer (Physical Electronics) equipped with a 180° spherical capacitor energy analyzer, at a base pressure of 5×10^{-7} mbar using monochromatic AlKα radiation (1486.68 eV). The binding energy scale was calibrated with the C 1s signal at 284.8 eV. The 3D geometry of the laser generated micro-probes was assessed by an X-ray microcomputed tomography (μCT) study. A RX EasyTom XL Ultra 160 device equipped with an open nano-focus tube was used at 60 kV acceleration voltage and 152 μA current. The distance between the source and detector was 400.204 μm with the specimen situated at 3.141 μm after the X-ray source. In total 1440 projections were gathered and the reconstruction done with the VGStudioMax software packet leading to a cubic voxel size of 996 nm with a total number of 1806 x 1806 x 1284 voxels in x, y, z directions. This allows measuring the probe with a micrometer resolution and resolve the complex 3D shape, shown in Figure S4. Additionally, a study on cross-sections machined with a plasma focused ion beam scanning electron microscope (PFIB-SEM) using Xenon ions was carried out. The Tescan Fera 3 device enabled to remove copper in fast manner whereas the SEM feature facilitated the alignment. Following, the geometry can be observed and analyzed which is in good agreement with the μCT measurements for the micro-probes assessed at different lengths, to be compared with Figure S4.

Computational modelling

The aim was to simulate the distribution of pH, CO_2 concentration, and fluxes of species involved in chemical equilibria within one individual micro-probe under the applied operating conditions. Dimensions are provided in Figure 1 and the origin of the z-axis was established at the base of the probes, with positive coordinates towards the interior. All experimentally obtained results arising from the combination of different lengths and applied potentials were modelled. In order to take into account both the influence of adjacent probes and the mild stirring resulting from CO_2 bubbling, the modelled domain comprised the electrolyte contained in the probe under study and the corresponding adjacent ones alongside a cylindrical volume of electrolyte, the height of which (50 μm) determines the distance at which bulk conditions apply, see Figure 4. This distance was estimated by calculating the thickness of a diffusion layer in a rotating disk experiment setup[5] at a mild rotation rate (200 rpm) resulting in characteristic values of electrolyte speed in the bulk of 0.5 cm s^{-1}, since diffusion was considered as the dominant mass transport mechanism. In the case of stirring, it was assumed a tangent speed of ca. 2 cm s^{-1}, corresponding to an equivalent rotation rate of 400 rpm, resulting in a Prandtl layer thickness of 180 μm, leading to an estimated diffusion layer thickness of ca. 20 μm. Sensitivity analyses discarded a strong sensitivity of simulated results with this value.

The reaction considered is the reduction of CO_2 and H_2O in 0.1 M $KHCO_3$ saturated with CO_2 (34.2 mM, pH 6.8) at 25 °C at −0.6, −0.8, −1.05, and −1.3 V vs. RHE toward products listed in Table S5, that contains those detected experimentally above trace levels. The considered bulk equilibria involving protonation/deprotonation of carbon species in solution and their corresponding forward and backward rate constants[1] are given in Table S6. The concentrations of H^+ and OH^- were considered to be all times in equilibrium and with negligible effect of the ionic strength, i.e., $C_H C_{OH} = 10^{-14}$. The diffusion coefficients D_j of involved species are reflected in Table S7. Under steady state, the equations 3-6 govern the mass balances of involved species.

$$\nabla \cdot (-D_{CO2} \nabla C_{CO2}) = k_{1r} C_{HCO3} - k_{1f} C_{CO2} C_{OH} \tag{3}$$

$$\nabla \cdot (-D_{HCO3} \nabla C_{HCO3}) = k_{1f} C_{CO2} C_{OH} - k_{1r} C_{HCO3} + k_{2r} C_{CO3} - k_{2f} C_{HCO3} C_{OH} \tag{4}$$

$$\nabla \cdot (-D_{CO3} \nabla C_{CO3}) = k_{2f} C_{HCO3} C_{OH} - k_{2r} C_{CO3} \tag{5}$$

$$\nabla \cdot (-D_{OH} \nabla C_{OH}) = k_{1r} C_{HCO3} - k_{1f} C_{CO2} C_{OH} + k_{2r} C_{CO3} - k_{2f} C_{HCO3} C_{OH} \tag{6}$$

The initial concentrations were calculated from the corresponding equilibria and are provided in Table S7. This group of equations must be complemented with the following set of boundary conditions.

Bulk conditions were considered at the free end of the cylindrical volume separated 50 μm from the base of the micro-probes (Table S7). A zero flux of species was imposed at the lateral wall of the cylindrical volume to reflect the symmetry of the array of micro-probes (equation 7).

$$-D_j \nabla C_j = 0 \text{ for } j = CO_2, HCO_3^-, CO_3^{2-}, \text{ and } OH^- \tag{7}$$

At the boundaries with the Cu surface a zero-flux condition was imposed on non-reactive species, equation 8.

$$-D_j \nabla C_j = 0 \text{ for } j = CO_2, HCO_3^-, CO_3^{2-} \tag{8}$$

For the species involved in the reduction of CO_2, the boundary condition was imposed as the flux of consumed/produced CO_2 and OH^- respectively according to the experimentally observed current densities and selectivity patterns under tested potentials. We assume a first-order dependence of the CO_2 consumption rate on the concentration (equation 9).

$$r_{CO2} = k_{CO2} C_{CO2} \tag{9}$$

Consequently, the boundary condition applied to the consumption of CO_2 on the Cu surface is given by equation 10.

$$D_{CO2} \nabla C_{CO2} = k_{CO2} C_{CO2} \tag{10}$$

The rate constant k_{CO2} is related to the total consumption of CO_2 on the walls of the electrode observed experimentally (equation 11),

$$\left(\frac{i}{F}\right)\sum_k \frac{FE_k n_k}{z_k} = \iiint_{walls} k_{CO2} C_{CO2} dxdydz \tag{11}$$

where the k index accounts for all observed carbon products, i represents the total current density measured, n_k and z_k represent the stoichiometric coefficients as reflected in Table S5. Similarly, the corresponding boundary condition for hydroxide must consider its production from the eCO$_2$RR and from the HER. The contribution from the eCO$_2$RR can be represented simply by the parallel equation 12,

$$\left(\frac{i}{F}\right)\sum_k \frac{FE_k m_k}{z_k} = \iiint_{walls} k_{OH,CO2R} C_{CO2} dxdydz \tag{12}$$

where m_k is the corresponding stoichiometric coefficient for the hydroxyl species in Table S5. A simple inspection of equations 11, 12, and Table S5 reveals that $k_{OH,CO2R}$ and k_{CO2} must be related linearly to each other. In regard to the HER contribution, we assume that the coverage of carbon species decreases as the CO$_2$ concentration does and that the local pH does not have a significant impact on the activity of Cu towards the HER at basic pH.[6] Based on this assumptions, we modelled the HER reaction rate as linearly dependent on the z-coordinate (equation 13),

$$r_{OH,HER} = k_{OH,HER} z \tag{13}$$

which leads to equation 14 accounting for the contribution of HER to the production of hydroxyl ions. In this regard, models assuming other HER dependency (i.e., decreasing or constant HER along the z-coordinate) resulted either in physically meaningless results or did not converge.

$$\left(\frac{i}{F}\right)\frac{FE_{H2} m_{H2}}{z_{H2}} = \iiint_{walls} k_{OH,HER} z dxdydz \tag{14}$$

At z=0, at the surface that was not laser drilled, the specific HER activity was assumed to be equal to the one observed over the LA-Cu-0 electrode at the corresponding potential (equation 15).

$$\left(\frac{i}{F}\right)\frac{FE_{H2} m_{H2}}{z_{H2}}\bigg|_{LA-Cu-0} = \iint_{z=0} k_{OH,HER,0} dxdy \tag{15}$$

Equations 13-15 lead to the boundary condition for the production of hydroxyl ions on the walls of the micro-probe (equation 16).

$$-D_{OH}\nabla C_{OH} = k_{OH,CO2R} C_{CO2} + k_{OH,HER} z \tag{16}$$

At z=0, the boundary condition is thus reflected by equation 17.

$$-D_{OH}\nabla C_{OH} = k_{OH,CO2R} C_{CO2} + k_{OH,HER,0} \tag{17}$$

The model included the local buffer effect of enhanced hydrolysis of cations (equation 18) next to the surface due to the electric potential following the description provided by Singh et al.[7]

$$\left[M^+(H_2O)_n\right] + H_2O \leftrightarrow \left[MOH(H_2O)_{n-1}\right] + H_3O^+ \tag{18}$$

The fast kinetics of these ionic reactions compared to the rate of formation of hydroxide ions due to the electrochemical processes allowed to consider them in equilibrium at the interface between the micro-probes and the electrolyte. Singh et al propose the pKa of the hydrolysis depends on the nature of the cation and comprise two terms accounting for the interaction of the cation with (i) the water molecules in the hydration sphere and (ii) the negative charge on the surface of the electrode, giving rise to equation 19.

$$pKa = -A\left[\frac{z^2}{r_w} + \frac{2\pi C N_A}{F} z V r_{surf}\left(\sqrt{1+\frac{r_w^2}{r_{surf}^2}} - 1\right)\right] + B \tag{19}$$

A (620 pm^{-1}) and B (17.154) correspond to fitted values, z is the effective charge of the hydrated cations (0.919 for K$^+$ and 0.930 for Cs$^+$), r_w is the sum of the radius of the cation and the oxygen atom (132 pm for K$^+$ and 148 pm for Cs$^+$), r_{surf} is the distance between the solvation sphere and

the electrode surface and is assumed to correspond to a CO molecule (250 pm), C is the specific capacity of the surface (51 µF cm^{-2} for Cu), and V denotes the cell voltage (Table S8). The reader is referred to ref[7] for a full description. The local buffer effect was introduced in the model by imposing the equilibrium reflected in equation 18 driven by equation 19 and the condition of zero flux for both hydrolyzed and partially dehydrolyzed cations at the boundaries with the Cu surface, as reflected in equation 20.

$$-D_j \nabla C_j = 0 \quad \text{for j} = M^+(H_2O)_n, MOH(H_2O)_{n-1} \tag{20}$$

Similarly, equation 18 was considered in equilibrium in the bulk of the solution disregarding the effect of applied potential (pKa = 14.5 for K$^+$ and pKa = 14.8 for Cs$^+$). The considered diffusion coefficients for K$^+$ and Cs$^+$ were 2.056 10^{-9} m^2 s^{-1} and 1.957 10^{-9} m^2 s^{-1}, respectively.[2]

The set of equations 3-6 with boundary conditions established by equations 7, 8, 10, 16, 17-20 alongside equations 11, 12, 14, 15 form a closed system, that was solved using a 3D finite element method incorporating a multifrontal massively parallel sparse direct solver (MUMPS) with a tolerance of 0.001 in the COMSOL® platform. The size of the unit element did not affect the values of the calculated variables significantly, confirming the mathematical robustness of the model.

Supplemental References

1. Gupta, N., Gattrell, M., and MacDougall, B. (2006). Calculation for the cathode surface concentrations in the electrochemical reduction of CO_2 in $KHCO_3$ solutions. J. Appl. Electrochem. *36*, 161–172.
2. Rumble, J.R. (2019). CRC Handbook of Chemistry and Physics. (Taylor & Francis).
3. Ackerl, N., Boerner, P., and Wegener, K. (2019). Toward application of hierarchical structures by ultrashort pulsed laser ablation. J. Laser Appl. *31*, 022501.
4. Ackerl, N., Warhanek, M., Gysel, J., and Wegener, K. (2019). Ultrashort-pulsed laser machining of dental ceramic implants. J. Eur. Ceram. Soc. *39*, 1635–1641.
5. Bard, A.J., and Faulkner, L.R. (2012). Electrochemical Methods - Fundamentals and Applications.
6. Raciti, D., Mao, M., and Wang, C. (2018). Mass transport modelling for the electroreduction of CO_2 on Cu nanowires. Nanotechnology *29*, 44001.
7. Singh, M.R., Kwon, Y., Lum, Y., Ager III, J.W., and Bell, A.T. (2016). Hydrolysis of Electrolyte Cations Enhances the Electrochemical Reduction of CO_2 over Ag and Cu. J. Am. Chem. Soc. *138*, 13006–13012.